RESEARCH ARTICLE

Frederik WIESMANN, Dong HAN, Zeyan QIU, Lukas STRAUβ, Sebastian RIEβ, Michael WENSING, Thomas LAUER

Numerical study of novel OME$_{1-6}$ combustion mechanism and spray combustion at changed ambient environments

Abstract For a climate-neutral future mobility, the so-called e-fuels can play an essential part. Especially, oxygenated e-fuels containing oxygen in their chemical formula have the additional potential to burn with significantly lower soot levels. In particular, polyoxymethylene dimethyl ethers or oxymethylene ethers (PODEs or OMEs) do not contain carbon-carbon bonds, prohibiting the production of soot precursors like acetylene (C_2H_2). These properties make OMEs a highly interesting candidate for future climate-neutral compression-ignition engines. However, to fully leverage their potential, the auto-ignition process, flame propagation, and mixing regimes of the combustion need to be understood. To achieve this, efficient oxidation mechanisms suitable for computational fluid dynamics (CFD) calculations must be developed and validated. The present work aims to highlight the improvements made by developing an adapted oxidation mechanism for OME$_{1-6}$ and introducing it into a validated spray combustion CFD model for OMEs. The simulations were conducted for single- and multi-injection patterns, changing ambient temperatures, and oxygen contents. The results were validated against high-pressure and high-temperature constant-pressure chamber experiments. OH*-chemiluminescence measurements accomplished the characterization of the auto-ignition process. Both experiments and simulations were conducted for two different injectors. Significant improvements concerning the prediction of the ignition delay time were accomplished while also retaining an excellent agreement for the flame lift-off length. The spatial zones of high-temperature reaction activity were also affected by the adaption of the reaction kinetics. They showed a greater tendency to form OH* radicals within the center of the spray in accordance with the experiments.

Keywords oxygenated fuels, reaction kinetics, oxidation mechanisms, computational fluid dynamics (CFD), oxymethylene ethers (OME), e-fuels, multi-injection, spray-combustion

Frederik WIESMANN (✉), Thomas LAUER
Institute of Powertrains and Automotive Technology, TU Wien, 1060 Vienna, Austria
E-mail: frederik.wiesmann@ifa.tuwien.ac.at

Dong HAN, Zeyan QIU
Key Laboratory for Power Machinery and Engineering of Ministry of Education, Shanghai Jiao Tong University, Shanghai 200240, China

Lukas STRAUβ, Sebastian RIEβ, Michael WENSING
Professorship for Fluid Systems Technology, Friedrich-Alexander-Universität Erlangen-Nürnberg, 91058 Erlangen, Germany

1 Introduction

The detailed investigation of possible future climate-neutral fuels is a prerequisite for any industrial application. Different pathways to produce renewable synthetic fuels are examined by Huang et al. [1], highlighting their advantages in high energy density, easy storage and transportation, and long-term storage compared to physical and electrochemical energy storage technology. Oxygenated synthetic fuels without C−C bonds combine the two essential aspects of CO_2 neutrality and soot-free combustion, thus enabling the solution of the soot-NO_x trade-off for diesel engines [2]. In recent years, polyoxymethylene dimethyl ethers (PODEs), alternatively called oxymethylene ethers (OMEs), were investigated intensively, confirming their potential as a transportation fuel for the reduction of soot emissions [3–6].

As the properties of OMEs like viscosity, lubricity, and boiling point depend on the quantity of oxymethylene ether groups (CH_2−O) within its chemical structure ($CH_3O(-CH_2-O)_n-CH_3$), it is found that OME$_{3-5}$ represents suitable surrogates for diesel fuel. It can be used purely or blended with diesel. Virt and Arnold [7] demonstrated lower particle emissions and shorter ignition delay times (IDTs) for diesel blends with up to 45 vol.% of OME$_{3-5}$ in a four-cylinder diesel engine. The

latter effect originates from the higher cetane number of OME_{3-5} compared to diesel.

Pélerin et al. [8] compared a neat OME_{3-6} fuel to paraffinic diesel fuel in a heavy-duty engine, identifying drastically reduced soot and particulate emissions, while retaining the same level of NO_x emissions. The tolerance against exhaust gas recirculation (EGR) was found to be very high, pointing to the potential to further reduce the NO_x emissions without the restrictions of a trade-off with soot or particle concentrations. The particle size distribution emitted by an OME_{3-6} fuel in a heavy-duty engine was analyzed by Gelner et al. [9], showing ultra-low levels of particle emissions independent of the usage of diesel particle filters or urea dosing. The measured particle number emissions were found to be smaller than for diesel. A detailed analysis of the influence of OME chain length on NO_x emissions was given by Dworschak et al. [10] on a single-cylinder diesel engine. A higher chain length was found to be beneficial in terms of NO_x emissions with only little drawbacks on thermal efficiency. The added benefit of reduced NO_x emissions was reported to outweigh the small reduction in engine efficiency for higher OME chain lengths.

The mixture formation of the same OME_{3-5} fuel mix, injector, and injection timing used in this study was analyzed and compared to n-dodecane and 1-octanol by Strauß et al. [11]. It was concluded that the mass distributions within the sprays of single injections were independent of the used fuel. Subsequent leaner or richer air−fuel equivalence distributions resulted from different air requirements of the fuels for stoichiometric conditions. For the multi-injection, the OME_{3-5} mix proved challenging as its relatively high density and low viscosity prolonged the opening time of the nozzle. Short pilot injections with a targeted injection time of 300 μs were too short for the injector to open completely.

Future industrial applications of OME_n necessitate an extensive knowledge of the ignition and combustion characteristics of this fuel. Wiesmann et al. [12] reported significant differences in simulated and experimentally determined ignition delay, flame morphology, and mixture formation between an OME_{3-5} fuel mix and n-dodecane in a constant pressure injection chamber. Numerical and experimental research conducted on an optically accessible single-cylinder engine showed similar results with shorter ignition delays and strong intensity levels of high-temperature reactions in the spray axis for OME_{3-5} when compared to n-dodecane [13].

The accurate prediction of IDTs, lift-off lengths, and other flame characteristics with the help of computational fluid dynamics (CFD) requires the utilization of optimized and validated oxidization mechanisms. Especially in Wiesmann et al. [12], it was concluded that the used reaction mechanism for the OME_{3-5} combustion, developed by Niu et al. [14], consistently underestimated the ignition delay and the intensity of high-temperature

reactions in the spray axis with changing ambient temperatures and oxygen contents. Lift-off length and flame propagation showed good agreement with the measurements, leading to the assessment that modifying the reaction mechanism can improve CFD results and, therefore, has a considerable potential.

This study aims to introduce an enhanced reaction mechanism for the oxidization of OME fuels with components ranging from OME_1 to OME_6. The new mechanism is validated with 0D-simulations against jet-stirred reactor (JSR) experiments conducted for this paper, as well as IDTs in shock tubes taken from the literature. The new mechanism is then applied to CFD calculations modeling a high-pressure, high-temperature, constant-pressure combustion chamber at changing ambient temperatures and oxygen contents with AVL FIRE®. The validation of the CFD simulations is achieved by OH*-chemiluminescence experiments. The reaction mechanisms used in the CFD simulations in this study do not consist of an excited OH* species but of unexcited hydroxyl (OH) as a species. Therefore, OH* is referenced for the experiments as the detected species, whereas the simulations track the OH mass fraction. The influence of multi-injection patterns with highly transient short pilot injections on the flame structure is analyzed. A particular focus is set on IDTs and the flame morphology in the spray axis.

2   Setup

2.1   Properties of OME fuel

The OME mix used in the present work is identical with the OME fuel used in Refs. [11–13], and is, hereinafter, referred to as OME. Its composition is shown in Table 1 [15], and its properties are described in Table 2 [15,16], derived from the OME batch analysis conducted by Analytik Service Gesellschaft (ASG) [15] and Pastor et al. [16].

The notation $(A/F)_{st}$ describes the air-to-fuel ratio at stoichiometric conditions. The remaining traces checked in the batch report of the fuel composition studied, other than OME groups, are sulfur (< 5 mg/kg), ash content (< 0.001 wt.%), and water (146 mg/kg).

Table 1   OME fuel composition

Molecule	Content/wt.%
OME_1	0.01
OME_2	<0.01
OME_3	57.90
OME_4	28.87
OME_5	10.07
OME_6	1.91

Table 2 Fuel properties of OME mixture

Property	Unit	Value
Density	kg/m^3 ($t = 15$ °C)	1057.10
Viscosity	mm^2/s ($t = 40$ °C)	1.08
Cetane number	–	68.6
Lubricity	μm	320
Flash point	°C	65
Lower heating value	MJ/kg	19.26
Initial boiling point	°C	144.40
Final boiling point	°C	242.40
Total contaminations	mg/kg	<1
Carbon content	wt.%	43
Hydrogen content	wt.%	8.53
Oxygen content	wt.%	46.4
(A/F)st at 21% of O$_2$	–	5.89:1
(A/F)st at 15% of O$_2$	–	8.18:1

Using an OME mix with components ranging from OME$_1$ to OME$_6$ ensures that the CFD validation process represents all relevant reaction pathways (Section 2.2) altered for the new oxidation mechanism.

2.2 Development of the new OME oxidation mechanism

Niu et al. [14] constructed an OME$_{1-6}$ reduced mechanism with a consistent reaction structure (including 92 species and 389 reactions). First, the OME$_{1-2}$ sub-mechanism was established using the decoupling methodology and sensitivity analysis (SA). The reaction classes of OME$_{3-6}$ sub-mechanism was derived from the OME$_2$ sub-mechanism, and the rate parameters were determined through the enhanced linear lumping method and analogy based on reaction rate rules. To validate the mechanism, comprehensive comparisons were conducted with experimental data from previous studies, such as IDTs in shock tubes, mole fraction profiles of key intermediates and products in JSR, burning velocity and flame species concentrations in premixed laminar flames, as well as in-cylinder pressures, heat release rates, and emissions in homogeneous charge compression ignition (HCCI) combustion. The results showed that the experimental data were predicted well by the current model.

The modification of the mechanism by Niu et al. [14], hereinafter referred to as the Niu mechanism, and the validation of the newly developed mechanism, hereinafter referred to as the Shanghai Jiao Tong University (SJTU) mechanism, is detailed in the following sections. At first, the experimental procedure using JSR is outlined. Next, the modifications to the Niu mechanism are described. Both mechanisms are then compared to the JSR experiments conducted for this study and with IDT data in the literature.

2.2.1 Experimental procedure of JSR

The OME mixture oxidation experiment is conducted on the JSR experimental platform. The oxidant is oxygen (99.99% purity), and the carrier gas is nitrogen (99.99% purity). The JSR used in this study has an internal volume of 75 cm^3 and an inner nozzle diameter of 0.3 mm. The reactor is placed in a heating furnace with a temperature control program, which can be heated to 1000 °C at most. A K-type thermocouple (OMEGA, TJ36-CAXL) monitors the real-time internal temperature of the reactor. The species detection and analysis system are a gas chromatograph (GC, Agilent 7890B). Gas chromatography is the most widely used detection and analysis technology in JSR experiments, which can quickly separate and identify various components in the mixed gas. In this study, the GC is outfitted with a thermal conductivity detector (TCD), allowing for the detection of permanent gases such as CO, CO$_2$, H$_2$, and O$_2$. The estimated uncertainty of measurements, considering reactant flow rates, temperature, calibration gases, and analytical equipment repeatability is approximately 10%.

The oxidation of OME blends is investigated at atmosphere pressure, temperature range of 500 to 900 K, and equivalence ratios of 0.5, 1.0, and 2.0. The temperature interval of each test point is 25 K. Two tests are conducted at each temperature point, and the reported value is determined as the average of the measured species concentrations. The initial fuel mole fraction and the residence time are fixed at 0.005 and 2 s, respectively.

During the experiments, the temperature of the fuel evaporation chamber is kept constant at 250 °C, which can vaporize OME fuel. All pipeline is kept at 100 °C to avoid an excessive temperature gradient and condensation. GC is used for the qualitative and quantitative detection of five substances, including O$_2$, CO, CO$_2$, H$_2$, and CH$_4$.

2.2.2 Mechanism modification and validation

First, the SA was performed to identify the important reactions. In the SA calculations of the IDT, the sensitivity coefficient is defined as

$$S = \frac{\tau(2.0k_i) - \tau(0.5k_i)}{1.5\tau(k_i)}, \qquad (1)$$

where S is the sensitivity coefficient, τ is the IDT, and k_i is the pre-exponential factor of the ith reaction.

In the SA calculations of mole fraction profiles, the OH radical was selected as the marked species because of its significant role in fuel combustion. The top ten reactions with higher absolute sensitivity coefficient were identified. Then, the rate constants of the important reactions were modified manually to obtain a better agreement with both JSR and IDT measurements.

Table 3 shows the modification details of the mechanism. The pre-exponential factor of the reactions numbered 313 and 314 were modified, mainly to reduce the difference between the model simulation and the JSR measurements in the mole fraction of essential intermediate products at about 600 K. The modification of reactions numbered 295, 311, 336, 361, and 386 is to decrease the predicted IDT.

Figure 1 shows the mole fractions of species measured in the oxidation experiments and provided by a kinetic simulation at the three equivalent ratios (0.5, 1.0, 2.0). The simulation is carried out in the closed zero-dimensional homogeneous reactor module using the Chemkin Pro software [17]. The OME mechanisms used in the simulation include the SJTU and Niu mechanisms to compare the prediction performances of these two mechanisms.

As shown in Fig. 1, the Niu and SJTU mechanisms can well capture the trend of mole fraction change at intermediate-to-high temperatures. However, it underestimates the O_2 mole fraction and overestimates the CO and CO_2 mole fraction at low temperatures. In contrast, the predictions from the SJTU mechanism align more closely with the mole fraction profiles across the three equivalence ratios and most temperature conditions. The SJTU mechanism predicts a lower oxygen consumption in the 500–600 K range, but a higher one in the 750–900 K range. For CO_2, the SJTU mechanism reduces the predicted value and the deviation from the experimentally observed values at 500–600 K. For CO, CO_2, and H_2, the SJTU mechanism improves the prediction quality at the temperatures of 750–900 K.

To ascertain the applicability and reliability of the newly developed mechanism, the IDTs of OME_3 reported in the literature are employed to verify the mechanism. Cai et al. [18] studied the spontaneous ignition behavior of $OME_{2–4}$ in a shock tube and measured the IDTs of an $OME_{2–4}$/air mixture in a series of initial conditions (10 and 20 bar pressure, 663–1137 K temperature range, equivalent ratio of 0.5, 1.0, and 2.0). Regarding the IDTs data of Cai et al. [18], the simulation in similar test conditions is carried out using the Niu mechanism and SJTU mechanism. The IDTs measured in the shock tube are generally short (0.01–2 ms), and the thermal change of fuel and oxidant mixture before ignition is small. An ideal constant volume combustion can approximate the whole combustion process. Therefore, the constant volume assumption is used to simulate the IDT of the shock tube. The instant when the OH concentration reaches the peak value during the ignition process is defined as the ignition time.

Figure 2 shows the measured IDT data at three equivalent ratios (0.5, 1.0, 2.0) and 10 and 20 bar pressure, comparing the simulation results of the two mechanisms. The results indicate that the SJTU mechanism improves the accuracy of predicting the IDT of OME_3/air. At the pressure of 20 bar, the results simulated from SJTU mechanism are closer to the experimental data in the 750–1000 K range at the equivalence ratio of 0.5 and 1.0. With an ambient pressure of 10 bar, the SJTU mechanism mainly reduces the IDTs calculated in the temperature range of 750–900 K and minimizes the deviation from the experimental values.

2.3 Operating points

The operating points for the spray combustion measurements and CFD simulations in the present work are presented in Table 4. The ambient density (ρ_{CC}) is kept constant at 22.8 kg/m^3. The primary focus is on the influence of temperature, oxygen content, and multi-injection pattern on the auto-ignition process. The temperature (T_{CC}) increases from 800 (OP1) to 900 K (OP2) and 1000 K (OP3). Additionally, the ambient volume content of oxygen in the combustion chamber is modified from 15% (OP2) to 21% (OP5). The multi-injection pattern is realized in the operating point (OP4).

2.4 Experimental setup

The experiments for investigating the fuel sprays are conducted using a high-temperature and high-pressure constant-volume injection chamber that is optically accessible. The test bench at the Professorship for Fluid Systems Technology (FST) is continuously scavenged with gas. The mixture can be adjusted from pure nitrogen to pure air, allowing reactive and inert investigations and

Table 3 Mechanism modification

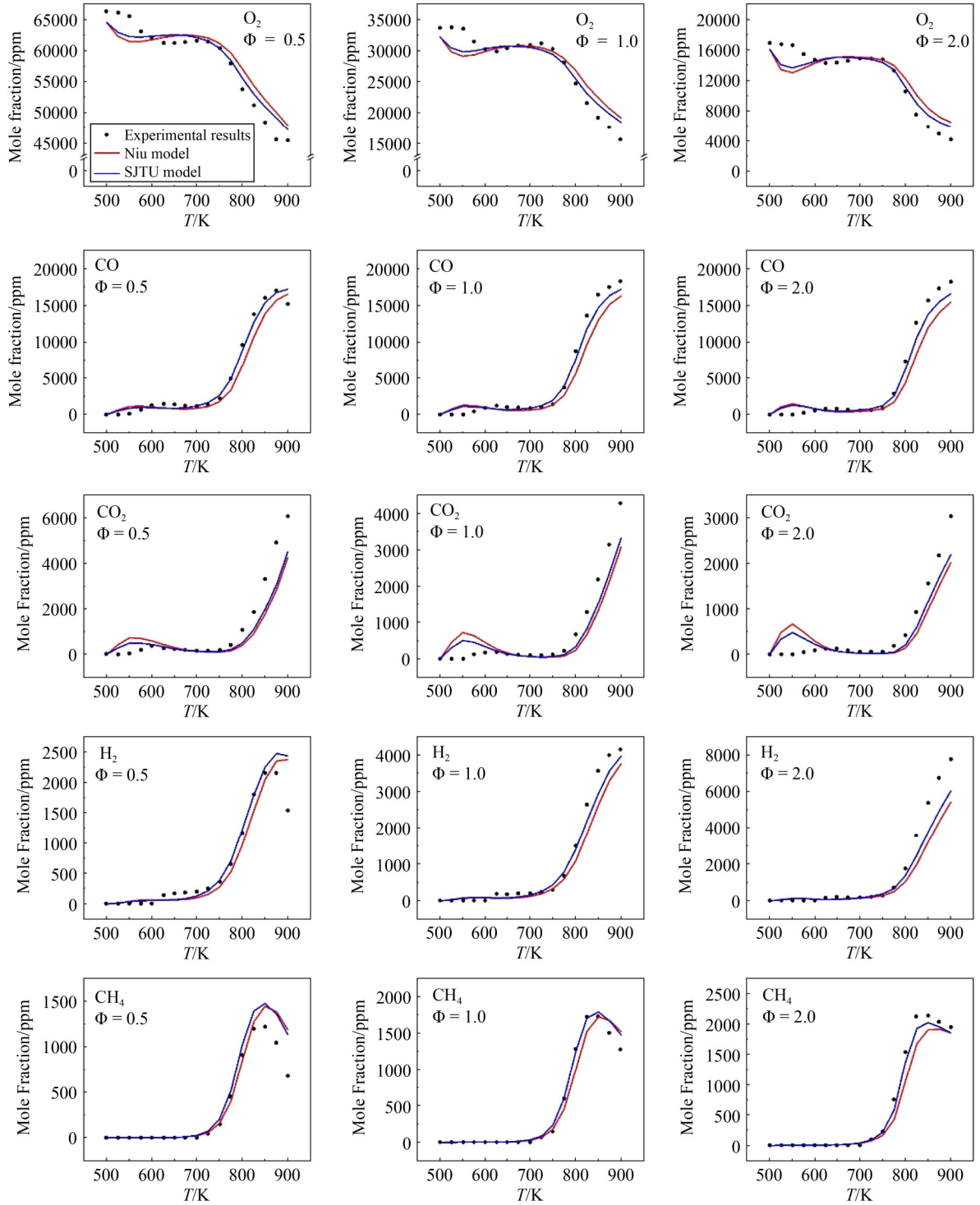| No.	Reaction	Modification
295	$OME_3 + HO_2 = OME3RX1 + H_2O_2$	$A_{295} \rightarrow 3A_{295}$
313	$CH_3OCH_2OCH_2OCHO + OH = HOCHO + CO + CH_3OCH_2 + H_2O$	$A_{313} \rightarrow 4A_{313}$
314	$CH_3OCH_2OCH_2OCHO + OH = 2CH_2O + CH_3O + CO + H_2O$	$A_{314} \rightarrow 6A_{314}$
311	$OME3X1OOHX3OO = OME3XKET1X3 + OH$	$A_{311} \rightarrow 0.5A_{311}$
336	$OME4X1OOHX3OO = OME4XKET1X3 + OH$	$A_{336} \rightarrow 0.1A_{336}$
361	$OME5X1OOHX3OO = OME5XKET1X3 + OH$	$A_{361} \rightarrow 0.1A_{361}$
386	$OME6X1OOHX3OO = OME6XKET1X3 + OH$	$A_{386} \rightarrow 0.1A_{386}$

Fig. 1 Measured and 0D-simulated O_2, CO, CO_2, H_2, CH_4 mole fraction profiles in OME oxidation (symbols: measurements; red lines: simulation results with the Niu mechanism; blue lines: simulation results with the SJTU mechanism).

the simulation of EGR. The gas temperature inside the chamber can be set from room temperature to 1000 K and is automatically controlled. The pressure can be regulated from 0.1 up to 10 MPa simultaneously. Both parameters are kept constant during the experiments. A research fuel system, compatible with different rails and injectors, provides the required fuel pressure up to 400 MPa.

Optical measurement techniques are used to obtain data about the fuel spray, its mixture, the ignition, and the combustion. The cubic chamber has windows on all sides (except where the injector is mounted) to allow high-speed imaging techniques. The optics are positioned to capture a side view of the fuel spray. The OH*-chemiluminescence is used to determine the
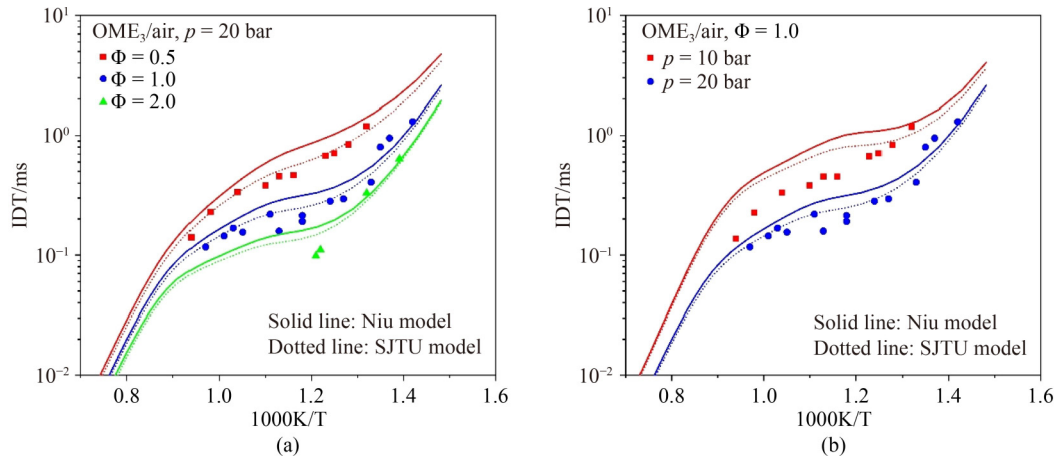
Fig. 2 Experimental and 0D-simulation IDT results of OME₃/air mixture in a shock tube (point: experimental measurement of Cai et al. [18]; solid line: simulation results with the Niu mechanism; dotted line: simulation results with the SJTU mechanism).
(a) Effects of equivalence ratio; (b) effects of pressure.

Table 4 Operating points

Label	Ambient temperature: T_{CC}/K	Ambient pressure: p_{CC}/bar	Ambient Density: ρ_{CC}/(kg·m⁻³)	Inj. temperature: T_{inj}/K	Inj. pressure: p_{inj}/bar	Inj. Duration: t_{inj}/ms	O₂-content/vol.%
OP1	800	54	22.8	363	1500	1.5	15
OP2	900	61	22.8	363	1500	1.5	15
OP3	1000	68	22.8	363	1500	1.5	15
OP4	900	61	22.8	363	1500	0.3/0.5/1.2	15
OP5	900	60	22.8	363	1500	1.5	21

ignition delay. To filter the OH* signal from the flame signal, a 307 ± 25 nm bandpass filter is used. The remaining radiation is focused on the high speed IRO X amplifier of LaVision using a 105 mm F/4.5 lens from Sill Optics. The amplified signal is then captured using a Photron SA-Z high speed camera at a framerate of 40000 fps (Fig. 3).

For each operating condition, 32 injections are performed, recorded, and analyzed using a purpose-built MATLAB-based program. The injected masses and mass flow rates are determined using the commercially available HDA 500 from Moehwald. This device consists of a pressurized volume filled with fuel, into which the injector injects fuel. The change in mass can be calculated by measuring the resulting pressure increase and the speed of sound within the volume. Integrating over the entire injection event leads to the total injected mass. For each operating point, 150 injections are recorded, and the results are subsequently averaged.

2.5 Injectors

This study shows experimental and numerical results for two different injectors, the Continental 3-hole injector (Conti3L) and the single-hole SprayA3 injector (see Table 5). Both injectors are described in more detail by Wiesmann et al. [12].
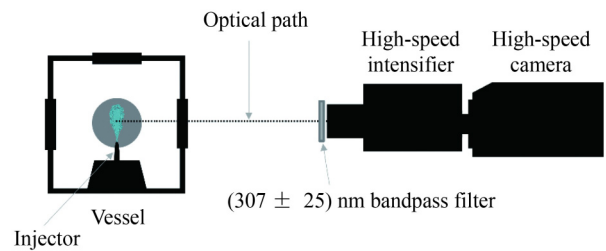

Fig. 3 Schematic of experimental OH*-chemiluminescence setup.

Table 5 Injector properties

Property	Conti3L	SprayA3
Orifice exit diameter/μm	115	97
Contraction coefficient (C_A)	0.98	0.98
Number of holes	3	1
Elevation angle/(°)	45	0

2.6 Numerical setup

The simulations of the present work are Reynolds averaged Navier–Stokes (RANS) equations calculations. The liquid droplets are modeled with a Lagrangian discrete droplet method (DDM) to track the liquid parcels throughout the numerical domain. In contrast, the

gaseous phase is modeled with a static Eulerian grid. The numerical setup used in this study was validated extensively by Wiesmann et al. [12].

2.6.1   Mesh

A simple spray-box mesh is utilized to determine the performance of the novel OME$_{1-6}$ reaction mechanism. The dimensions of the mesh are 120 mm in length and 60 mm in width. Three refinements up to a minimum cell size of 125 μm are implemented and described in Table 6 [12] and shown in Fig. 4. The notations R1 and R2 signify the radii at beginning and end of the respective refinement. The fine resolution of the mesh ensures converged calculations for both phases, liquid and gaseous, especially in the vicinity of the nozzle hole. The refinements chosen ensure that, for both injectors, the liquid phase evaporates within the area of the highest resolution for all operating points. Minimizing the cell size even further does not show any improvement regarding the quality of the results, while only pushing the necessary simulation time to unjustifiable limits. The boundary opposite to the nozzle is set as a non-reflecting outlet. All other mesh boundaries are set up as walls with fixed temperatures.

2.6.2   Submodels

This chosen turbulence model within the RANS framework for this study is the k-ζ-f turbulence model [19]. The near wall regions are modeled with a compound wall treatment described by Popovac & Hanjalic [20]. The pressure correction is done with the SIMPLE algorithm with an additional correction using the standard pressure-implicit with splitting of operators (PISO) formulation.

The chosen fuel injection pressure of 1500 bar results in high injection velocities. During injection, the temporal resolution is set to 0.5 μs to ensure the satisfaction of the Courant criterion with the given fine mesh. After the injection ended, the time step is increased to 1.0 μs.

The introduction of the liquid parcels is realized with the Blob method [21], initializing liquid blobs continuously with the same size as the effective nozzle hole diameter. The primary and secondary droplet breakup is simulated with the Kelvin-Helmholtz-Rayleigh-Taylor (KHRT) breakup model [21,22]. The OME mix used in the present work comprises multiple components (see Table 1). This requires an evaporation model of the liquid parcels capable of accounting for a multi-component fuel. Therefore, the model described by Brenn et al. [23] is used, an enhancement of the model by Abramzon & Sirigano [24], treating the mass transfer from liquid droplet to gaseous phase separately for every component. Table 7 summarizes the numerical models[12,13].

Determining the transient liquid injection rates used for the spray modeling within this study follows the same methodology described in by Wiesmann et al. [12]. In particular, the ramp-up and ramp-down phases while opening and closing the injector cannot be deducted straightforwardly from standard experiments with long-tube type instruments (HDAs) described in Section 2.4. In Pickett et al. [27], it was shown for the Spray A injector that mechanical vibrations lead to an overestimation of rate fluctuations and that the initial ramp-up is underestimated.

Consequently, the present work models the rates of injection with virtual rates of injection, which differ from the experimentally determined ones. Figure 5 depicts both the virtual injection rates for single and multi-injection of the injectors. For the Conti3L injector, the HDA experiments already provide an average for the three nozzle holes. The steady-state phase between ramp-up and ramp-down transients is modeled by replicating the mean value per nozzle hole of the HDA experiments. The SprayA3 injector is characterized by unsteady behavior even between the ramp-up and ramp-down transients. Therefore, the standardized method published by the Polytechnical University of Valencia [28] was used to generate the injection rates for SprayA3 injector. The generated rates for the CFD calculations clearly show a faster ramp-up and ramp-down than the profiles

Table 6   Mesh refinement

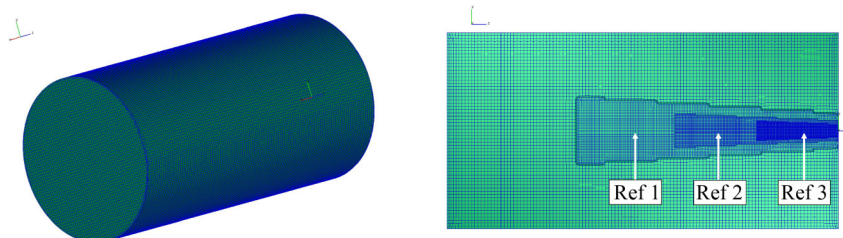| Refinement	L/mm	R1/mm	R2/mm	Cell size/mm
0 (base mesh)	120	30	30	1.000
1	80	5	10	0.500
2	50	3	5	0.250
3	25	2	3	0.125

Fig. 4   Spray-box mesh with cut-through center plane visualizing refinement levels.

Table 7 Summary of numerical submodels

	Injection type	Blob [21]
Liquid spray models	Breakup	KHRT [21,22]
	Turbulent dispersion	O'Rourke & Bracco [25]
	Evaporation	Brenn et al. (multi-component) [23]
	Drag Law	Schiller-Naumann [26]
Gaseous phase models	Temporal discretization	0.5 μs (during injection); 1.0 μs (after injection)
	Turbulence modeling	RANS approach; k-ζ-f model [19]
	Wall treatment	Compound (hybrid) [20]
	Pressure-correction	SIMPLE (1st) / PISO (2nd)
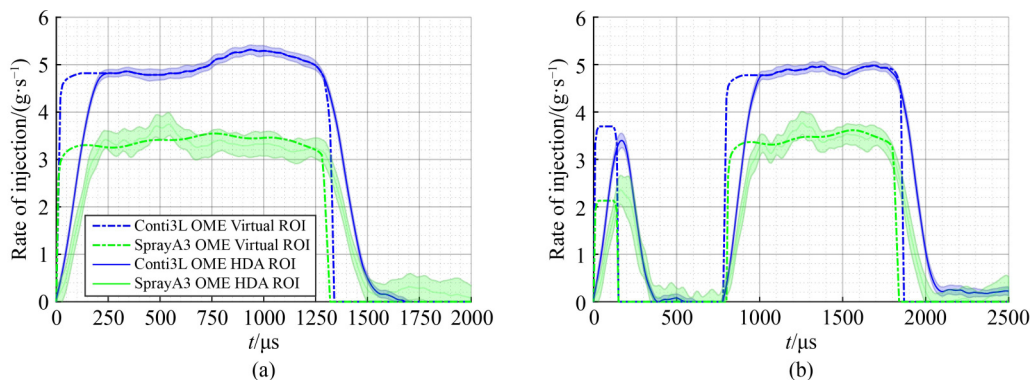
Fig. 5   Rates of injection (ROI) for numerical input (p_{inj} = 1500 bar, p_{CC} = 60 bar).
(a) Single injection; (b) multi-injection.

measured by the HDA flowmeter.

The most challenging aspect is the adequate modeling of the highly transient pilot injection for the multi-injection operating point (OP4, Table 4). The pilot injections do not comprise any steady-state phase but are entirely dominated by the ballistic operating conditions the injector is forced into. In Peter et al. [29], it was shown that the fuel properties, i.e., relatively high density and low viscosity, of an OME_3 and OME_4 mix directly influence the needle motion and, consequently, the mass flow rate development. This observation was also confirmed by Strauß et al. [11] with the same OME_{3-5} mixture, SprayA3 injector, and injector timing as in the present work. For the short pilot injection, the opening process of the needle was found to take significantly longer for OME_{3-5} compared to *n*-dodecane and 1-octanol. Furthermore, the OME_{3-5} mixture led to the injector not even opening completely.

The maximum velocity of the spray during the pilot injection can be calculated by the method presented by Frühhaber et al. [30] using the conservation of momentum along the spray axis. This method allows for the generation of accurate injection rates.

2.6.3   Combustion modeling

The modeling of the OME fuel oxidization is conducted

by applying the detailed reaction mechanisms for every time step. The gas phase reactions in AVL FIRE® treat every computational cell as a well-mixed homogeneous reactor. To increase the accuracy of the simulations, turbulence chemistry interaction (TCI) is considered. Its implementation via a Gaussian presumed probability density function (pPDF) applied to the local temperature is described in detail in AVL List Gmbh [31] and has been already utilized by Wiesmann et al. [12]. However, the impact of the TCI for the CFD simulations of the present work is very small. It does not affect the lift-off length and has only a minor influence on the IDT. The different reactions kinetics used in this study result in changes for the lift-off length and ignition delay which are at least an order of magnitude greater. The high resolution of the computational mesh is assumed to minimize the influence of the TCI.

The mixing state of fuels is usually defined by the equivalence ratio (ϕ) (Eq. (2)). However, it was found by Mueller [32] that the existence of chemically bound oxygen in fuels leads to an overestimation of the distance from stoichiometric ratios. This results in mixtures appearing to be significantly farther away from stoichiometry than they are in reality. Hence, a new formulation was described by Mueller [32] to eradicate this error. The so-called oxygen equivalence ratio (ϕ_{Ω}) is defined in Eq. (3) for the case that neither C- nor

H-atoms is present in the oxidizer. The term Ω_f describes the oxygen ratio of the fuel. It is a property of the fuel itself, representing "the number of O-atoms per mole of fuel divided by the number of O-atoms required to convert all C- and H-atoms of the fuel in a mole of fuel to saturated stoichiometric products [32]". It is specified in Eq. (4). The subscript i in Eq. (4) denotes the index over all fuel species, and a_i describes the number of moles of the ith fuel species. For this study, the OME fuel mix has an oxygen fuel ratio of $\Omega_{f,OME} = 0.2566$.

$$\phi = \frac{m_f/m_{ox}}{(m_f/m_{ox})_{st}}, \tag{2}$$

$$\phi_\Omega = \frac{\phi}{1 + \Omega_f \cdot (\phi - 1)}, \tag{3}$$

$$\Omega_f = \frac{\sum_i a_i n_{O,i}}{\sum_i a_i \left(2n_{C,i} + \frac{1}{2}n_{H,i}\right)}, \tag{4}$$

The super- or subscripts f and ox indicate the respective element mass fraction within the fuel and oxidizer. In addition to the newly developed reaction mechanism for simulating the oxidization of OME, described in Section 2.2 and the original mechanism published by Niu et al. [14], calculations were performed with the mechanism by Cai et al. [18]. This reaction scheme only incorporates oxymethylene groups extending from two to four (OME$_2$ to OME$_4$), whereby the components OME$_5$ and OME$_6$ of the OME mix used are dismissed. It considers 322 species for the oxidation of OME.

---

3   Results

In this section, the results of the novel OME reaction mechanism are shown in comparison with the original one developed by Niu et al. [14]. At first, the global quantities ignition delay and flame lift-off length are analyzed in Section 3.1. Furthermore, the flame morphology, especially the spatial and temporal distribution of the low- and high-temperature reactions characterized by formaldehyde (CH$_2$O) and OH, are presented in Section 3.2. The differences in the mixing regimes due to applying the novel reaction mechanism are shown in Section 3.3. For each analysis, single and multi-injection patterns are considered.

3.1   Ignition delay and lift-off length

For identifying the IDT, this study utilizes the standard definition of Engine Combustion Network (ECN) [33], specifying the start of combustion for CFD calculations as the moment of the greatest temperature gradient. The lift-off length is based on a threshold of the OH mass fraction of 14 percent. The nearest axial downstream distance where this threshold is exceeded, determines the lift-off length. The penetration of the flame front is calculated by evaluating the maximum distance from the nozzle where the mixture fraction satisfies the condition of $Z \geq 0.001$. Equation (5) describes the calculation of the mixture fraction with Z_i specifying element mass fractions of the ith element.

$$Z = \frac{Z_i - Z_i^{ox}}{Z_i^f - Z_i^{ox}}. \tag{5}$$

Both ignition delay and flame lift-off length are validated against OH*-chemiluminescence experimental data. The measured IDT is determined as the first detection of an OH*-signal in at least half of the conducted experimental repetitions. According to Riess et al. [34], the evaluated signal probability determines the IDT.

3.1.1   Single injection

For the first validation of the spray combustion model utilizing the novel SJTU reaction mechanism, the IDT is plotted against the lift-off length in Fig. 6 for the standard ECN operating of 900 K chamber temperature at an oxygen content of 15% (OP2 in Table 4). Next to the novel SJTU mechanism, the original Niu mechanism and the reaction mechanism developed by Cai et al. [18] were employed to simulate the OME spray combustion. The shown standard deviations of the measurements were derived from 32 injection repetitions for each operating point. The standard deviations for the simulated lift-off length were determined by averaging the calculated lift-off after a stable flame was established and before the end of injection. Figure 13 visualizes the same period for OP2 (see Table 4) for averaging the CH$_2$O and OH distribution discussed in Section 3.2.1.

The SJTU mechanism increases the IDT for both injectors while retaining the same lift-off length as the Niu mechanism. The more detailed Cai mechanism, consisting of 322 species, also yields an increased IDT, albeit while overestimating the lift-off length. The significant overestimation of the lift-off length by the CFD calculations using the mechanism of Cai et al. [18] leads to a flame morphology that cannot capture the shape of the flame seen in the experiments. Therefore, it was concluded that the Niu mechanism has a greater potential for modification than the Cai mechanism.

Hereinafter, the SJTU mechanism will be compared directly to the original Niu mechanism. The general trend of overestimating the lift-off length when predicting the ignition delay more accurately was analyzed in the case of n-dodecane and OME serving as fuels by Wiesmann et al. [12]. Therefore, the fact that the new SJTU mechanism achieves a better prediction of the ignition delay and a good agreement with the measured lift-off

length is already a significant improvement.

The same conclusion can be drawn from analyzing other operating points that vary in chamber temperature (Fig. 7) and oxygen content (Fig. 8). For all investigated cases, the SJTU mechanism predicts the IDT with a very good accuracy. The lift-off length is only slightly affected compared to the Niu mechanism, maintaining a good agreement with the measurements.

The elongation of the ignition delay for the SJTU mechanism is more pronounced at lower temperatures. For an alternating oxygen content, the ignition delay is shifted toward greater values for the SJTU mechanism with the same relative difference between the two

mechanisms. It is also illustrated in Fig. 8 that the measured deviation in the ignition delay for the two injectors at 900 K chamber temperature could not be reproduced by the CFD model.

3.1.2 Multi-injection

The highly transient injection profile for the multi-injection pattern (see Fig. 5), with its short pilot injection, causes ignition of the OME spray during the dwell period of the injector. The top two plots in Fig. 9 indicate the time-resolved development of the maximum temperature within the entire simulation domain, with the vertical
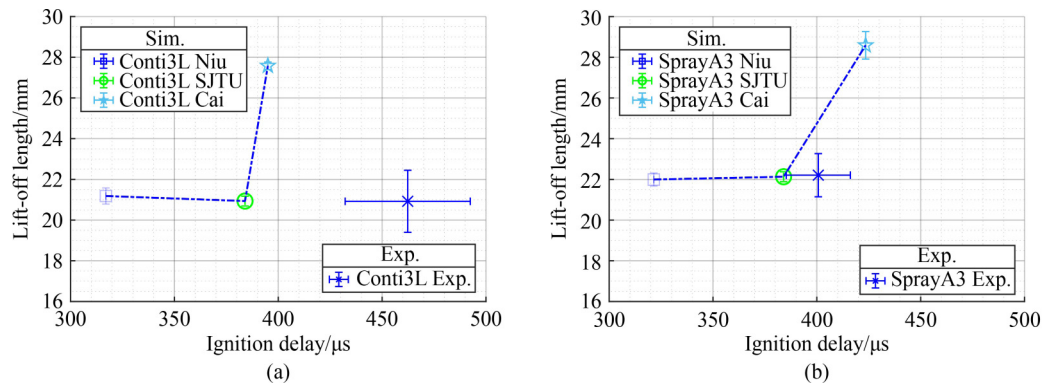
Fig. 6 Lift-off length versus ignition delay for different reaction mechanisms for OP2 (900 K and 15% O_2).
(a) Conti3L injector; (b) SprayA3 injector.
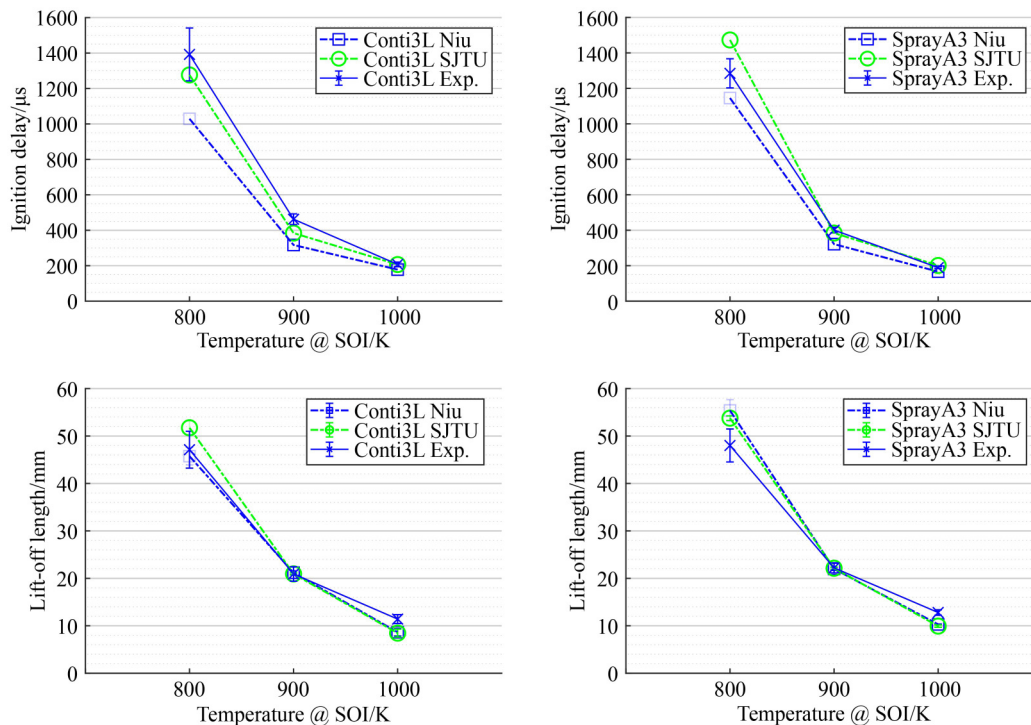
Fig. 7 Comparison of Niu and SJTU reaction mechanism for temperature sweep at 15% O_2.
(left) Conti3L injector; (right) SprayA3 injector; (top) ignition delay; (bottom) lift-off length.
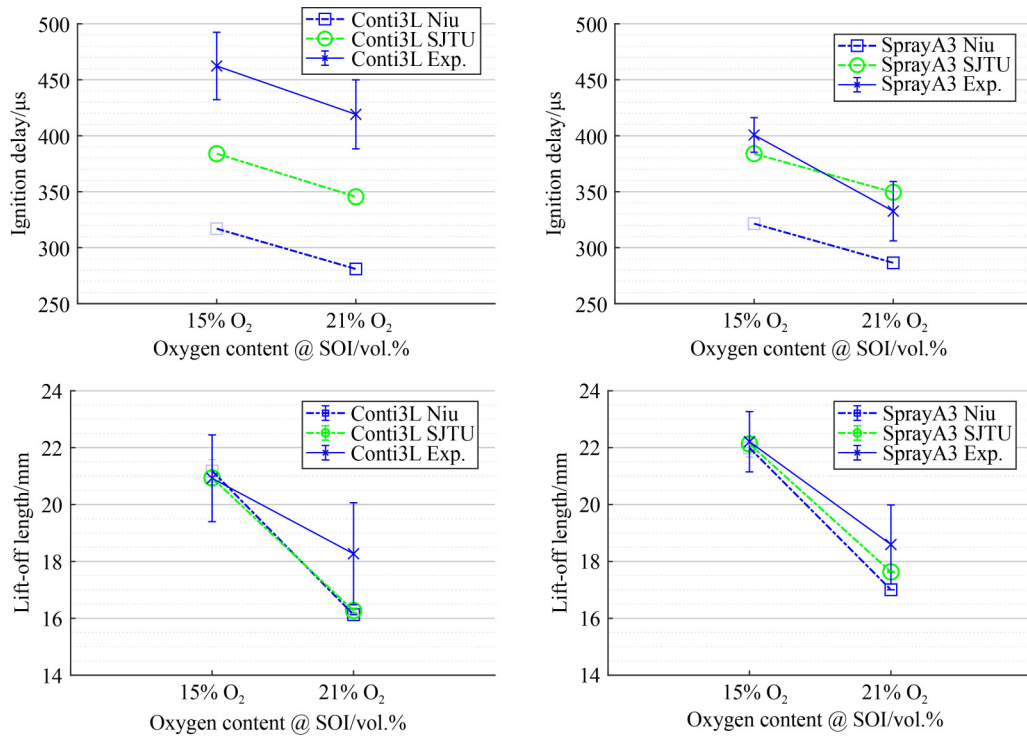
Fig. 8 Comparison of Niu and SJTU reaction mechanism for oxygen content sweep at 900 K.
(left) Conti3L injector; (right) SprayA3 injector; (top) ignition delay; (bottom) lift-off length.
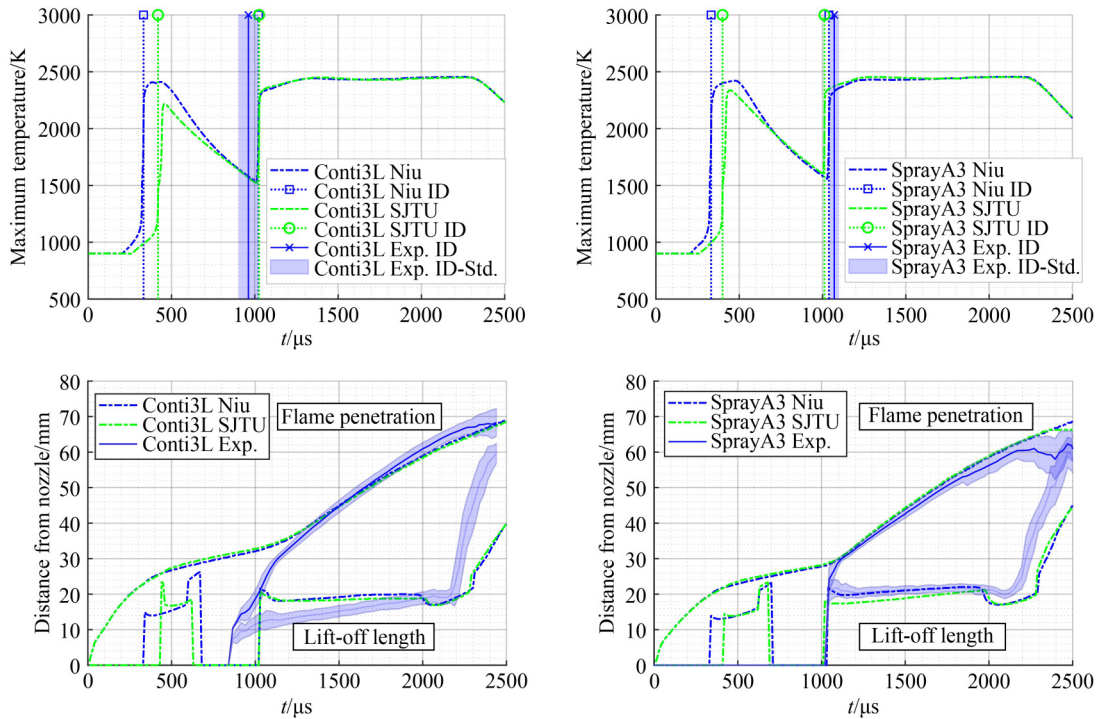

Fig. 9 Transient profiles for multi-injection.
(left) Conti3L injector; (right) SprayA3 injector; (top) maximum simulation temperature with ignition delay (ID); (bottom) lift-off length and flame (mixture fraction) penetration.

lines signaling the ignition. The CFD simulation predicts an ignition for both mechanisms shortly after the pilot injection ended. A distinctive re-ignition of the spray is noticeable after a rapid decline in simulated maximum temperature and the subsequent start of the main injection. However, the experiments could not validate this behavior as no ignition was detected before the main injection. This behavior was already reported by Wiesmann et al. [12], using the same CFD and experimental setup, speculating that either a too-reactive OME mechanism (Niu) or a too-weak OH*-signal resulting from the small amount of OME introduced into the spray chamber during the pilot injection is causing this discrepancy between simulation and experiment. The occurrence of the same ignition pattern calculated with the less-reactive SJTU mechanism, causing a longer ignition delay, indicates that the weak OH*-signal is the reason for this observation. The difference in the ignition delay predicted for the two reaction mechanisms for the main injection changes only a little for the SprayA3 and not at all for the Conti3L injector.

Following the observation from the single injection, the flame penetration and lift-off length remain virtually unaffected by the updated reaction mechanism, depicted in the bottom two plots in Fig. 9. The flame penetration was calculated with the condition of the mixture fraction (Eq. (5)) reaching the threshold of $Z \geqslant 0.001$.

3.2   Flame morphology

For the analysis of the shape and structure of the OME spray combustion flame, the low-temperature and high-temperature reactions are studied. The former is characterized by the formation and subsequent decomposition of CH_2O. The latter is dominated by the emergence of OH, which can be validated against the experimental data yielding qualitative results about the location and distribution of OH* via chemiluminescence.

All simulated distributions are presented for the symmetry plane of the spray. For an adequate comparison to the simulated results, the OH*-chemiluminescence measurements were deconvoluted to obtain the OH* signal distribution in the symmetry plane of the spray for each time step, following the methodology described by Peter [35]. Hereby, the integral flame signal is converted into a three-dimensional object using tomographic reconstruction. Intensity values from the flame can then be transferred to the symmetry plane of the flame assuming rotational symmetry.

The analysis considers the operating points with single (OP2) and multi-injection patterns (OP4) at a chamber temperature of 900 K and an oxygen content of 15 vol.%. The detailed transient evolutions of the CH_2O and OH distributions are shown for both injection strategies, differentiating the low- from the high-temperature reaction zones. The measurements and simulations are also averaged over time for the single injection to deliver a more precise and compact comparison between the two reaction mechanisms. The averaging period is set to start after a stable lift-off length is established, at 500 μs after the start of injection (SOI), and to end before the subsiding injection rate starts to influence the flame at 1350 μs.

3.2.1   Single injection

The first aspect of the analysis of the flame morphology is the comparison of the reaction rates and mass fractions for CH_2O and OH for the two reaction mechanisms under investigation. The values are averaged over all cells, yielding the profiles shown in Fig. 10.

At first glance, it is discernible that the SJTU mechanism produces higher levels of CH_2O throughout the combustion process. The reaction rate of CH_2O consists of a higher initial burst and is elevated during the steady-state phase of the OME spray injection (500 μs < t_{aSOI} < 1350 μs). This results in a significantly higher predicted mean mass fraction in the simulation domain. The SJTU mechanism shows a more minor initial burst of the OH reaction rate. Shortly after high-temperature ignition, though, the mean mass fraction and the OH reaction rate no longer differ between the two reaction mechanisms. The start of significant production for both species, CH_2O and OH, is shifted toward later during the combustion process. On a closer look into Fig. 10, it is also recognizable that the delay between the onset of CH_2O and OH production is slightly longer for the SJTU mechanism, further adding to the increased ignition delay described in Section 3.1.1

The difference in CH_2O production leads to the transient analysis of the CH_2O distribution maps for both mechanisms. Figure 11 illustrates the temporal evolution of the molar concentration of the simulations with the Niu and the SJTU mechanisms in a slice through the center of the SprayA3 injector. The time interval was shortened in proximity to the ignition delays for both mechanisms (ID_{Niu} = 321.5 μs and ID_{SJTU} = 384.0μs). Stoichiometric mixing conditions (ϕ_Ω = 1) are plotted into the contours as black solid iso-lines. To distinguish between the low-temperature cool-flame contour, characterized by CH_2O, and the areas of the high-temperature flame, characterized by OH, the high-temperature front of 1400 K is tracked by magenta solid iso-lines. According to Tagliante et al. [36], the consumption of CH_2O occurs approximately at this temperature.

The initial production of CH_2O occurs along the lines of stoichiometry for both mechanisms, only shifted to a later time after injection for the SJTU mechanism. Elevated levels of CH_2O concentration form on the
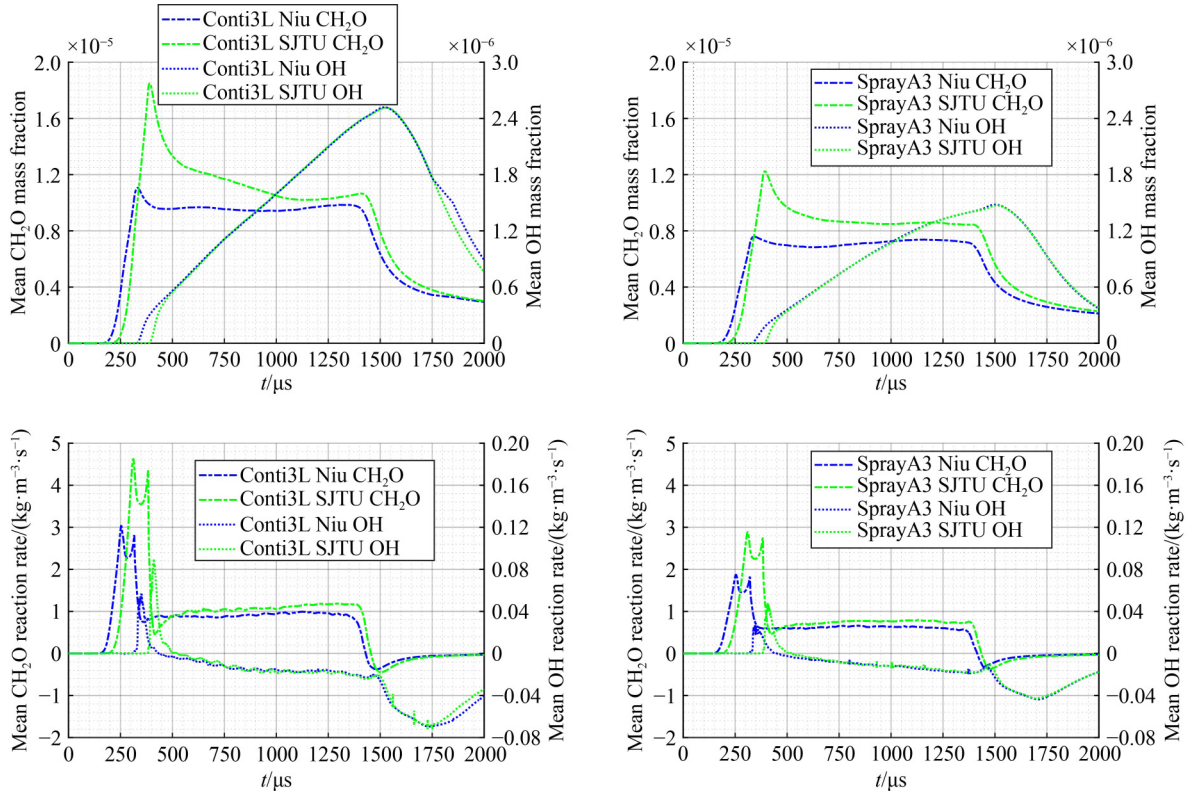
Fig. 10   Transient profiles for CH$_2$O and OH for single injection.
(left) Conti3L injector; (right) SprayA3 injector; (top) mean mass fractions; (bottom) mean reaction rates.

centerline of the spray approximately 20 to 30 μs before ignition. It is noticeable that the SJTU mechanism accumulates more CH$_2$O before igniting at the cool-flame front. In addition, high levels of CH$_2$O concentration reach further upstream along the centerline of the spray. These observations reflect the higher plateau of CH$_2$O mean mass fractions seen in Fig. 10. After ignition, the high-temperature reactions consume the CH$_2$O within the area enclosed by the magenta lines, showing the temperature front of 1400 K.

After inspecting the cool-flame evolution, Fig. 12 depicts the temporal development of the high-temperature flame, characterized by OH*-intensity for the experiments and the molar concentration of the OH species for the simulations. To ensure a better comparison, simulations and experiments are normalized with their respective maximum value for the displayed time step. Both mechanisms capture the general shape and spatial dimensions of the high-temperature flame. The SJTU mechanism shows a slightly higher activity in the centerline of the spray. However, it is still insufficient compared to the high intensity measured at the center of the OME spray. Both mechanisms overestimate the reaction activity in the shear layer of spray and ambient air. Especially within the initial stages of combustion, the SJTU mechanism seems to be able to capture the experimentally observed high-temperature flame better

than the Niu mechanism, probably due to the improved and prolonged ignition delay and the greater accumulation of CH$_2$O in the center of the spray prior to ignition. The slight improvements in the SJTU mechanism diminish as the injection process continues, leading to a similar high-temperature flame distribution at one millisecond after SOI. The experimentally observed high intensity of OH* near the nozzle at the root of the spray is not reproduced by either reaction mechanism. One possible explanation for this behavior is that the experiments measure the excited OH* signal, which is very volatile and quickly consumed by the high-temperature reactions. This is compared to the presumably more stable OH mass fraction of the simulations, as neither the Niu nor the SJTU mechanism comprises an excited OH species for a more adequate comparison to the experiments.

To better compare the differences between the two mechanisms, the spatial distributions of the cool-flame (CH$_2$O) and high-temperature (OH) contours were averaged once a stable flame lift-off could be detected. Figure 13 depicts the flame penetration and lift-off length for OP2, indicating the averaging period. For both injectors, the flame stabilizes around 500.0 μs after SOI, entering the quasi-steady period in terms of flame lift-off.

The reactive front, tracked by the mixture fraction threshold of $Z \geqslant 0.001$, propagated approximately 34 mm
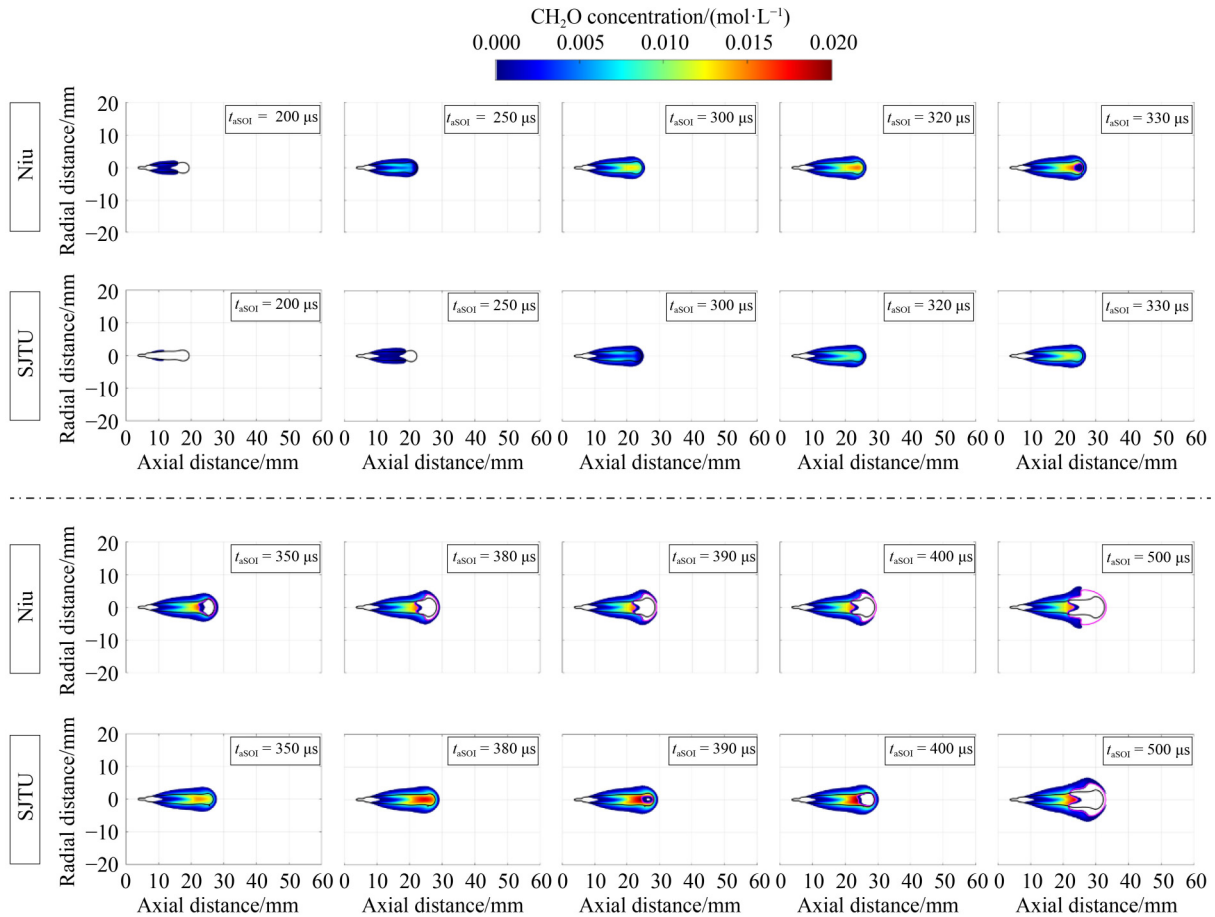
Fig. 11 SprayA3-OP2 (900 K and 15% O_2): CH_2O molar concentration contours in the center plane for single injection (black lines depict stoichiometric mixing, and magenta lines show the temperature front of 1400 K).
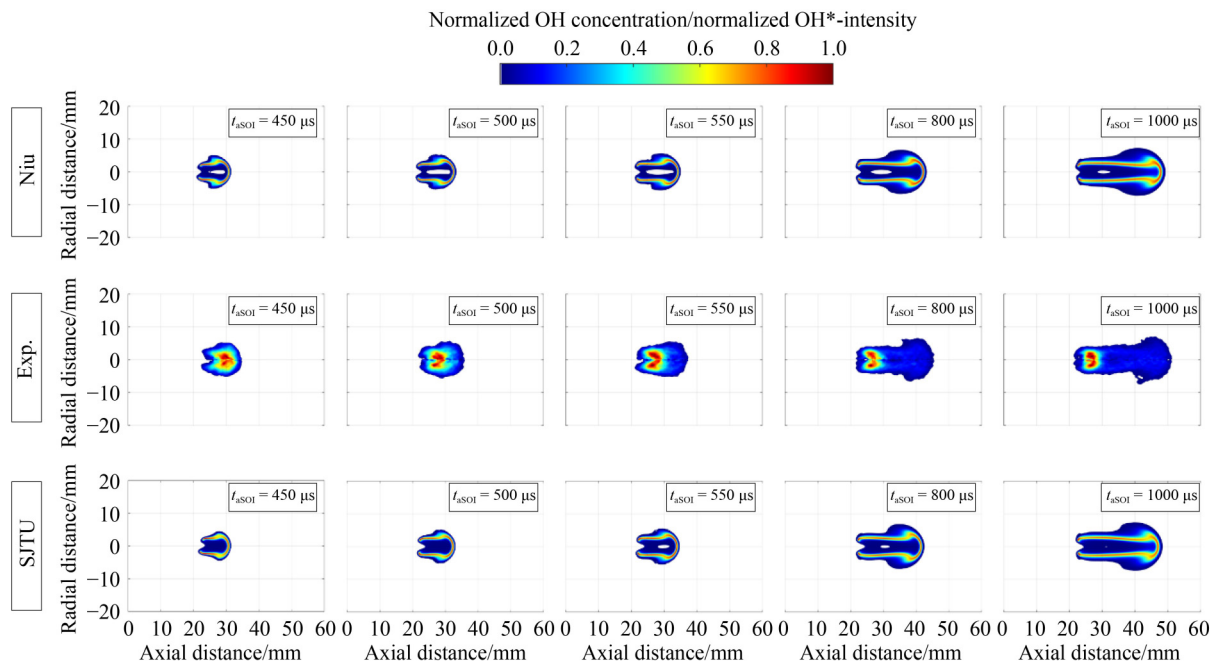

Fig. 12 SprayA3-OP2 (900 K and 15% O_2): normalized OH*-intensity (experiment) and OH molar concentration (simulation) contours in the center plane for single injection.

for simulations and experiments for both injectors. Figure 11 clearly shows that the CH$_2$O is consumed 30 mm downstream of the nozzle, which means the averaging process captured the entire CH$_2$O field present in the simulation. However, the averaging process affects the OH/OH* averaged results for simulations and experiments downstream of 34 mm as the flame front is still propagating. As simulations and experiments are averaged by the same method, comparisons are

nevertheless considered valid.

As the experiments showed that most of the high-temperature flame activity occurred in the center of the spray, the centerline profiles of the CH$_2$O and OH were of interest for a detailed comparison of the two mechanisms. The top two plots of Fig. 14 display the differences between the SJTU and Niu mechanisms in accumulating CH$_2$O in the center axis of the spray, with the SJTU mechanism amassing significantly more CH$_2$O
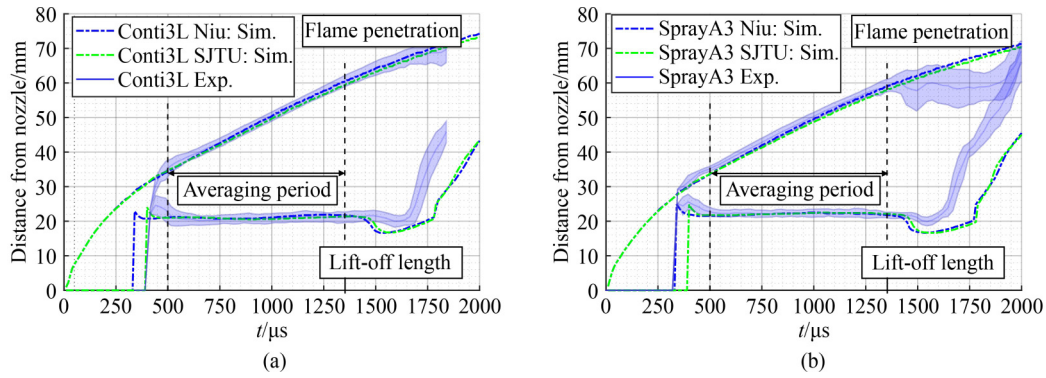
Fig. 13   Transient profiles for lift-off length and mixture fraction penetration and time-averaging period indication for OP2 (900 K and 15% O$_2$) single injection.
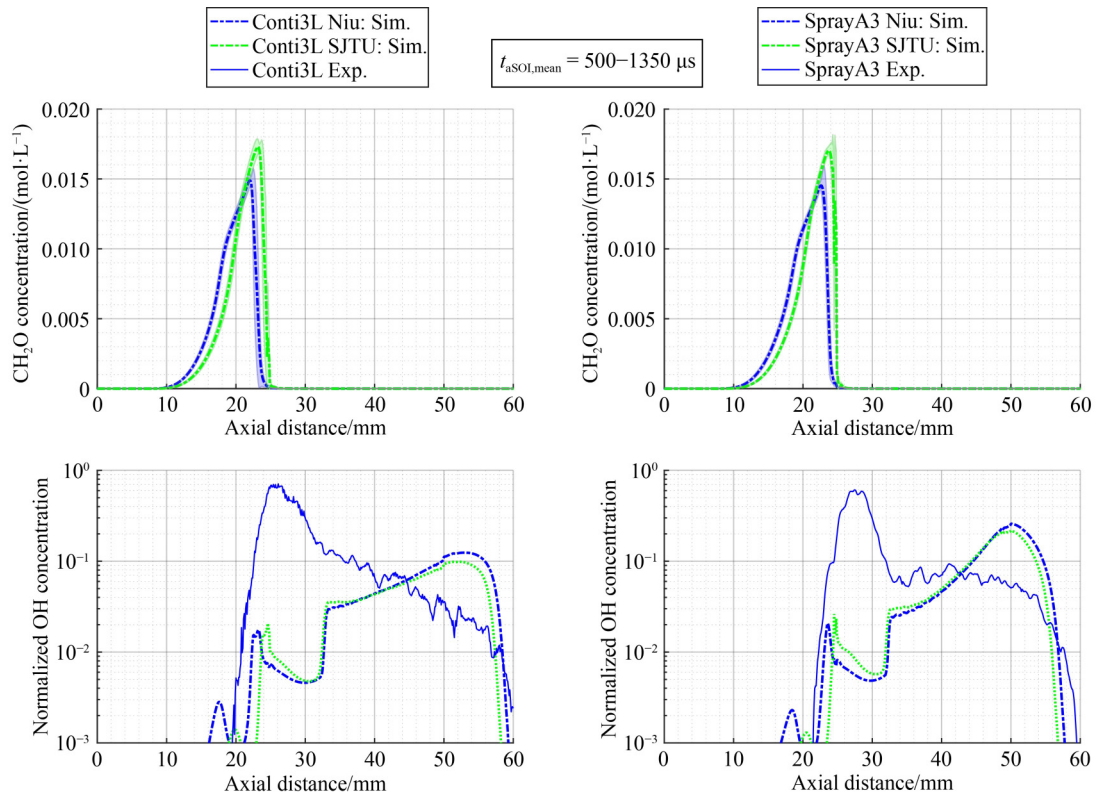
(a) Conti3L injector; (b) SprayA3 injector.

Fig. 14   Time-averaged centerline profiles for OP2 (900 K and 15% O$_2$) single injection.

(left) Conti3L injector; (right) SprayA3 injector; (top) CH$_2$O molar concentration; (bottom) normalized OH concentration (simulation) and OH*-intensity (experiment) with logarithmic ordinate.

in the center slightly downstream of the calculated lift-off length. The OH/OH* profiles at the center axis of the spray are shown in the bottom two plots of Fig. 14 with a logarithmically plotted ordinate. The concentration of OH*-intensity at the center axis of the spray, measured by the experiments, cannot be reproduced by either mechanism. The higher CH_2O accumulation for the SJTU mechanism in the center translates to only slightly greater OH concentration downstream of the flame lift-off. At the tip of the averaged profile, the Niu mechanism exceeds the SJTU one in OH concentration, which also signals an improvement for the novel mechanism compared to the experiments.

To improve the visualization of the OH distribution of the simulations in comparison with the OH*-intensity of the experiments, radial profiles at axial positions a few millimeters downstream of the steady-state lift-off length are shown in Fig. 15, again with a logarithmic ordinate. The deviation between experiments and simulations in the center axis is visible for all positions. Still, there is also a slight increase in the levels of OH concentration for the SJTU mechanism. As no axial positions beyond 30 mm were evaluated, the averaging process did not affect the results shown in Fig. 15.

Compared to the differences seen for the CH_2O centerline profile and maps, the differences in OH formation between the two mechanisms are significantly smaller. This indicates that the transition from low-temperature (CH_2O) to high-temperature (OH) flame remains the key area for further improvements regarding the reaction kinetics modeling for OME spray combustion.

3.2.2 Multi-injection

The approach in analyzing the two mechanisms in the case of the multi-injection event follows the same logic as for the single injection, however, focusing on the transient development of the flame during the short pilot injection. At first, the global mass fractions and reaction rates of CH_2O and OH, characterizing the cool-flame and high-temperature reactions, respectively, are compared in Fig. 16. The pilot injection is characterized by a higher plateau of CH_2O formation for the SJTU mechanism. For the main injection, this is only the case for the Conti3L injector simulations, delivering a more complex picture than the single injection in Fig. 10. The formation of OH after the ignition of the pilot injection is barely noticeable for the SJTU mechanism, suggesting that a reaction mechanism with an even longer ignition delay might eventually lead to the pilot injection not igniting at all. Another observation from Fig. 16 is that the delay between the beginning of the CH_2O and the OH production is increased for the SJTU mechanism.

The transient development of the distribution of molar concentration of CH_2O is plotted in Fig. 17 for a slice through the center plane of the SprayA3 injector. The top half of each plot represents the calculation with the Niu mechanism, and the bottom half shows the SJTU mechanism simulation. As for the single injection case, stoichiometric mixing conditions are visualized as black solid lines. The area where high-temperature reactions consume the CH_2O is indicated in each plot with magenta solid lines tracking the temperature front of 1400 K.

The earlier ignition of the Niu mechanism is shown, as well as the ignition in the center of the spray at fuel-rich conditions within the boundary set by the black lines of stoichiometric mixing. The flame expands outwards simultaneously when the stoichiometric area starts to shrink until it vanishes entirely due to the small amount of OME injected. This outward expansion process is initiated for the SJTU mechanism when almost the entire mixture is lean. This suggests that the pilot ignition for
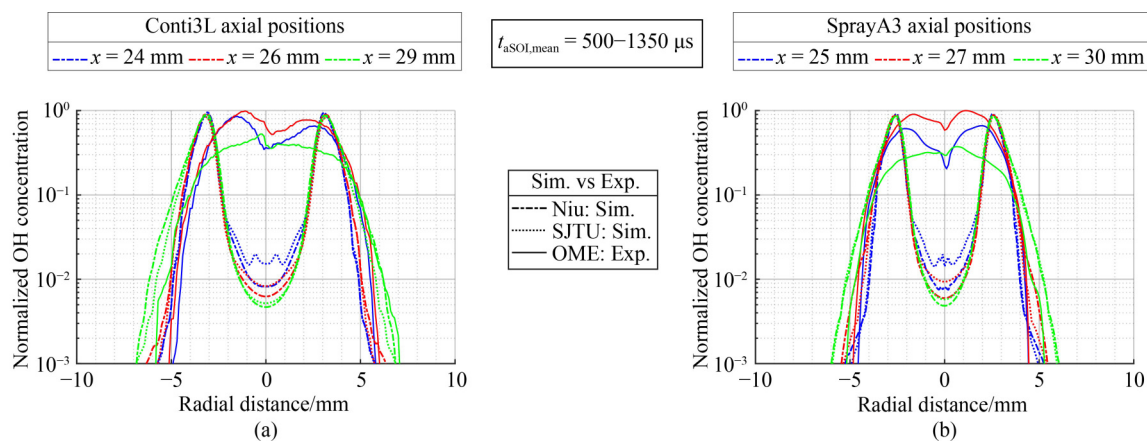

Fig. 15 Time-averaged OH radial profiles for single injection after stable lift-off length is established for OP2 (900 K and 15% O_2) single injection.
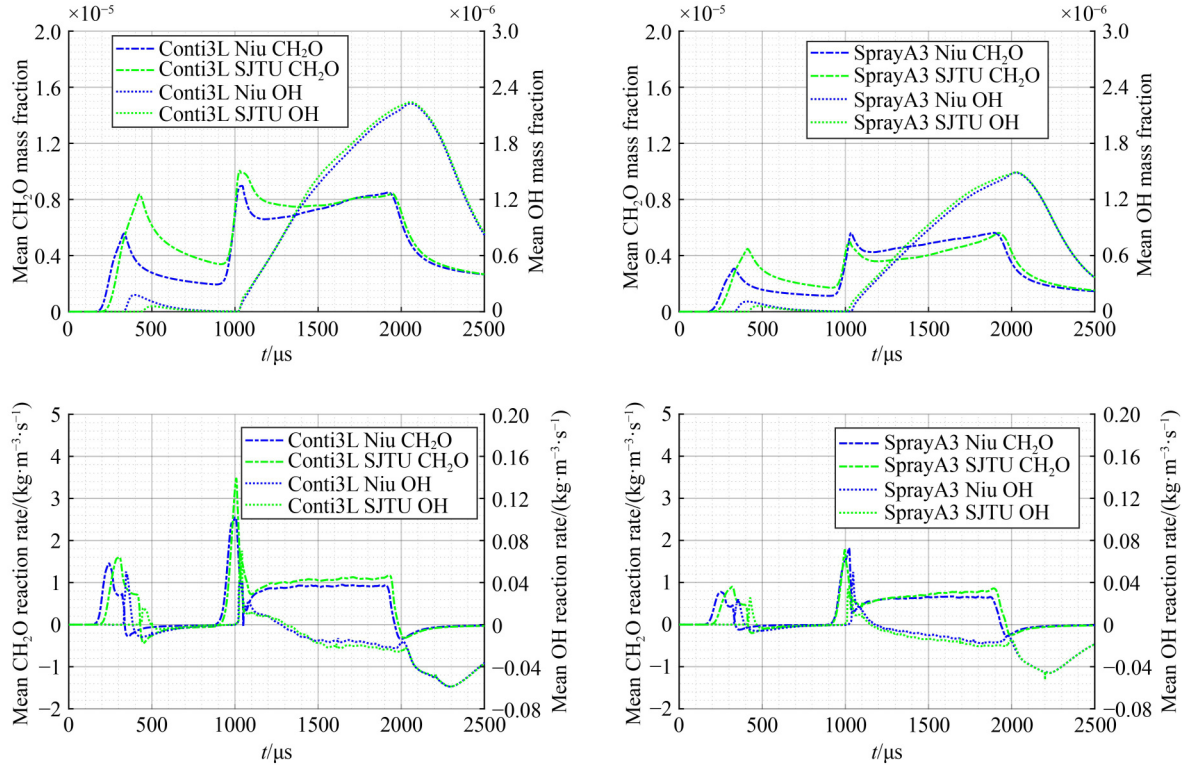
(a) Conti3L injector; (b) SprayA3 injector.

Fig. 16 Transient profiles for CH$_2$O and OH for multi-injection.
(left) Conti3L injector; (right) SprayA3 injector; (top) mean mass fractions; (bottom) mean reaction rates.

the SJTU mechanism occurs in very lean conditions. The delay of ignition and increased accumulation of CH$_2$O throughout the pilot injection is visible for the SJTU mechanism.

At the end of the pilot injection, the high-temperature flame detaches from the cool flame. It is eventually merged with the reignited spray of the main injection, which develops a high-temperature flame at the spray tip, reaching further upstream along the line of stoichiometric mixing.

The flame reaches farther back upstream for the SJTU mechanism, resulting in a slightly shorter lift-off length already visualized in Fig. 9. The ignition within the mixing field created by the pilot injection differs from the single injection in that there is no significant and consistent difference in ignition delay (of the main injection) and that the accumulation of CH$_2$O at this elevated temperature does not vary substantially between the two reaction mechanisms.

In Fig. 18, the planar contours of the concentration of the OH species and OH*-intensity for the measured data are plotted for the pilot and main injection. The ignition of the pilot injection is concentrated in the spray center for both mechanisms, albeit more evenly distributed in the case of the SJTU mechanism. The experiments could not detect an OH*-signal for the pilot injection. Only the main injection generated a string-enough signal so that

the OH*-intensity could be processed into qualitative plots showing the intensity distribution of the high-temperature flame. As for the cool flame characterized by CH$_2$O, the high-temperature reaction activity does not differ significantly between the two mechanisms. Both mechanisms underestimate the reaction activity within the center axis of the spray. The elevated temperatures and the mixing field resulting from the ignition of the pilot injection impede the improvements otherwise noticeable for the new SJTU mechanism.

3.3 Mixing regimes

In Wiesmann et al. [12], spray combustion simulations with the Niu mechanism and the same OME mix did not produce any mixing states, which could be considered as potentially forming soot. The limits for an increased soot yield are defined by equivalence ratio and temperature. According to Refs. [37,38], the equivalence ratio, or in the case of oxygenated fuels like OME, the oxygen equivalence ratio (ϕ_Ω, see Eq. (3)), needs to exceed two ($\phi_\Omega \geqslant 2$). The temperature range of $1200\,\text{K} \leqslant T \leqslant 2000\,\text{K}$ to form soot is set by the need for radical precursors such as acetylene (C$_2$H$_2$) or C$_3$H$_3$ [39]. Below that, these precursors do not exist, and above 2000 K, they are pyrolyzed and oxidized. Figure 19 illustrates scatter plots, with each dot representing one simulation cell with the
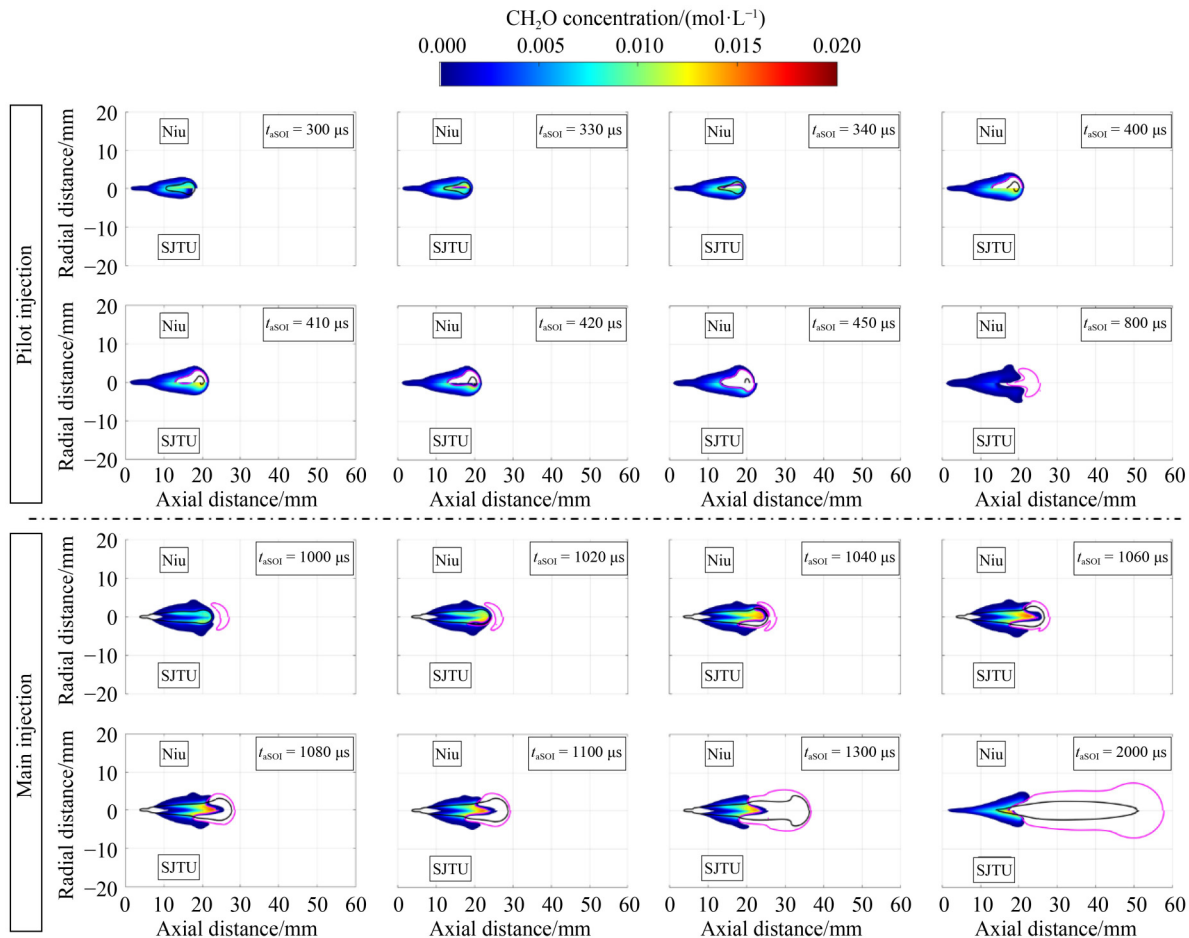
Fig. 17 SprayA3-OP4 (900 K and 15% O_2): CH_2O molar concentration contours in the center plane for multi-injection (black lines depict stoichiometric mixing, and magenta lines show the temperature front of 1400 K).

(top) the Niu mechanism; (bottom) the SJTU mechanism.

increased soot yield region indicated within the plots as gray boxes. The top two plots have all simulation cells scaled with their respective OH mass and colored with their OH mass fraction. In the bottom plots of Fig. 19, each cell is scaled with its CH_2O mass and colored with its respective CH_2O mass fraction.

This visualization enables one to differentiate the low- and high-temperature combustion within the given time step of t_{aSOI} = 1000 μs. Both mechanisms do not come close to mixing regimes that potentially form soot. The combustion for this snapshot in time for the SJTU mechanism seems slightly leaner. The OH high-temperature stage of the combustion process does not differ substantially between the two reaction mechanisms. It is centered around temperatures above 1500 K, and most of the OH production occurs in an area close to stoichiometric conditions. However, the cool-flame CH_2O occurrence differs from the SJTU mechanism to the Niu mechanism. The temperature range of CH_2O production is similar for both mechanisms, but for the SJTU one, CH_2O is present in leaner conditions,

with the highest observed CH_2O mass fractions reaching back to oxygen equivalence ratios smaller than unity ($\phi_\Omega < 1$).

A simple way to capture the entire transient combustion process and not only a snapshot in time is to focus on the simulation cell with the maximum temperature. Figure 20 displays the maximum temperature of the simulation plotted against its corresponding oxygen equivalence ratio. For the single injection, top plots in Fig. 20, leaner combustion can be identified. For the multi-injection, bottom plots in Fig. 20, the profiles are split into pilot and main injection. A significant difference between the two oxidization mechanisms can be recognized for the pilot injection, as the SJTU mechanism ignites in very lean conditions with equivalence ratios smaller than unity ($\phi_\Omega < 1$). This observation coincides with Fig. 16, showing little OH production for the pilot injection ignition when using the SJTU mechanism. Both mechanisms experience a rapid cool-down after the pilot injection and follow a similar trend once the main injection starts. However, even
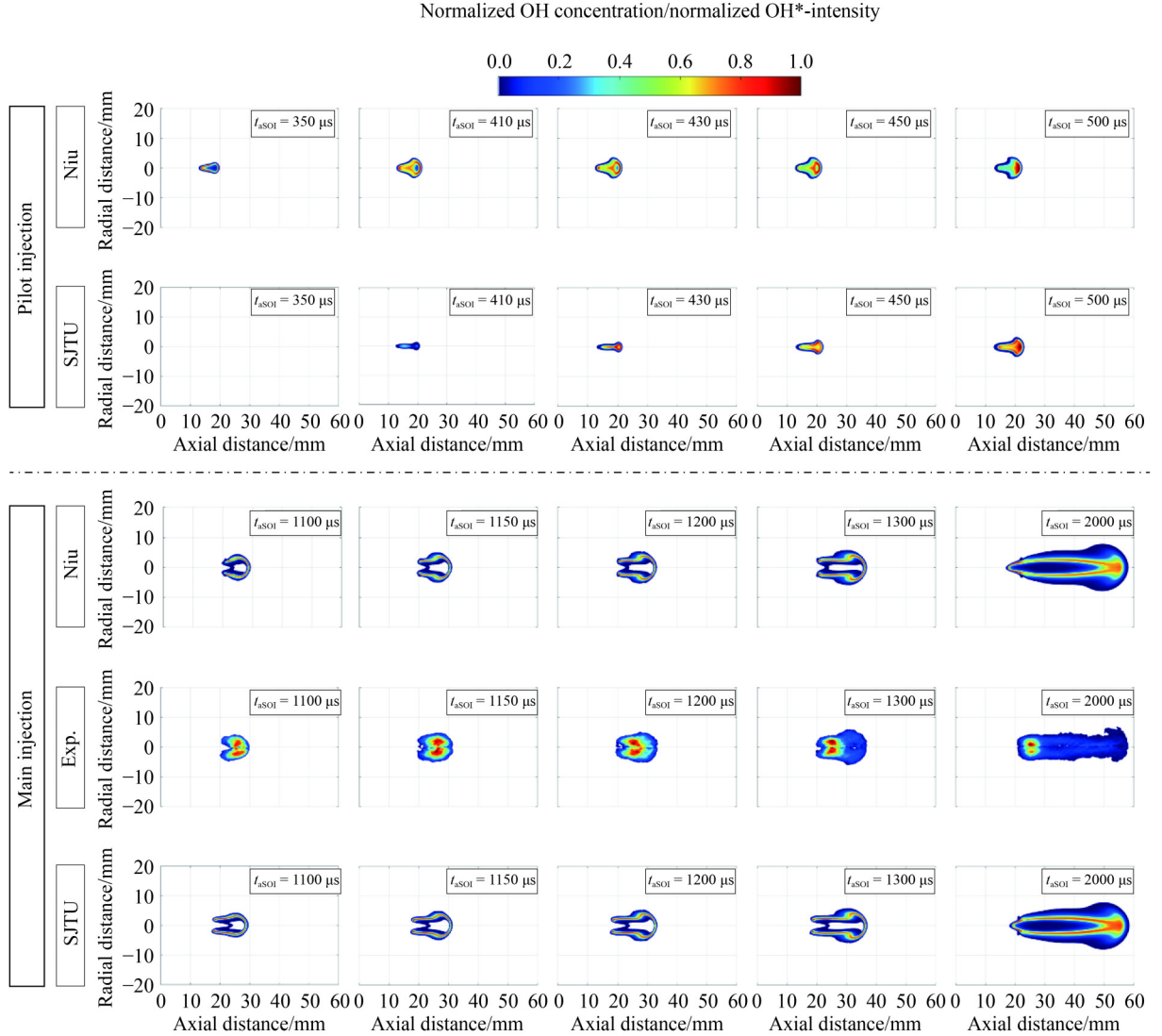
Fig. 18 SprayA3-OP4 (900 K and 15% O$_2$): Normalized OH*-intensity (experiment) and OH molar concentration (simulation) contours in the center plane for multi-injection and SprayA3 injector.
(top) the Niu mechanism; (bottom) the SJTU mechanism.

during the main injection, a slightly leaner combustion for the SJTU mechanism is revealed.

4 Conclusions

The presented study analyzed the impact of a novel reaction mechanism suitable for CFD simulations describing the oxidization of PODE or OME with a chain length of $n = 1$–6 (OME$_{1-6}$). At first, the new oxidization mechanism (SJTU mechanism), based on the work of Niu et al. [14] (Niu mechanism), was utilized in a 0D homogeneous reactor model. The mole fractions simulated were compared to JSR experiments. The new reaction mechanism was shown to predict the measured data for CO, CO$_2$, O$_2$, and H$_2$ with a higher accuracy over

a range of equivalence ratios and temperatures compared to the original mechanism. Furthermore, the IDTs reported by Cai et al. [18] for OME$_3$ in air were utilized to validate the 0D-simulated ignition delays by the SJTU and Niu mechanisms. The results yielded that the SJTU mechanism consistently performed better in predicting the ignition delay.

The CFD simulations were validated against OH*-chemiluminescence experimental data within an optically accessible constant-volume injection chamber. The main conclusions describing the improvements achieved with the new SJTU mechanism for OME are:

1) The quality of the IDTs predicted by the SJTU mechanism is significantly improved for a temperature range of at least 800–1000 K and oxygen content levels of 15% and 21%. The lift-off length and flame front
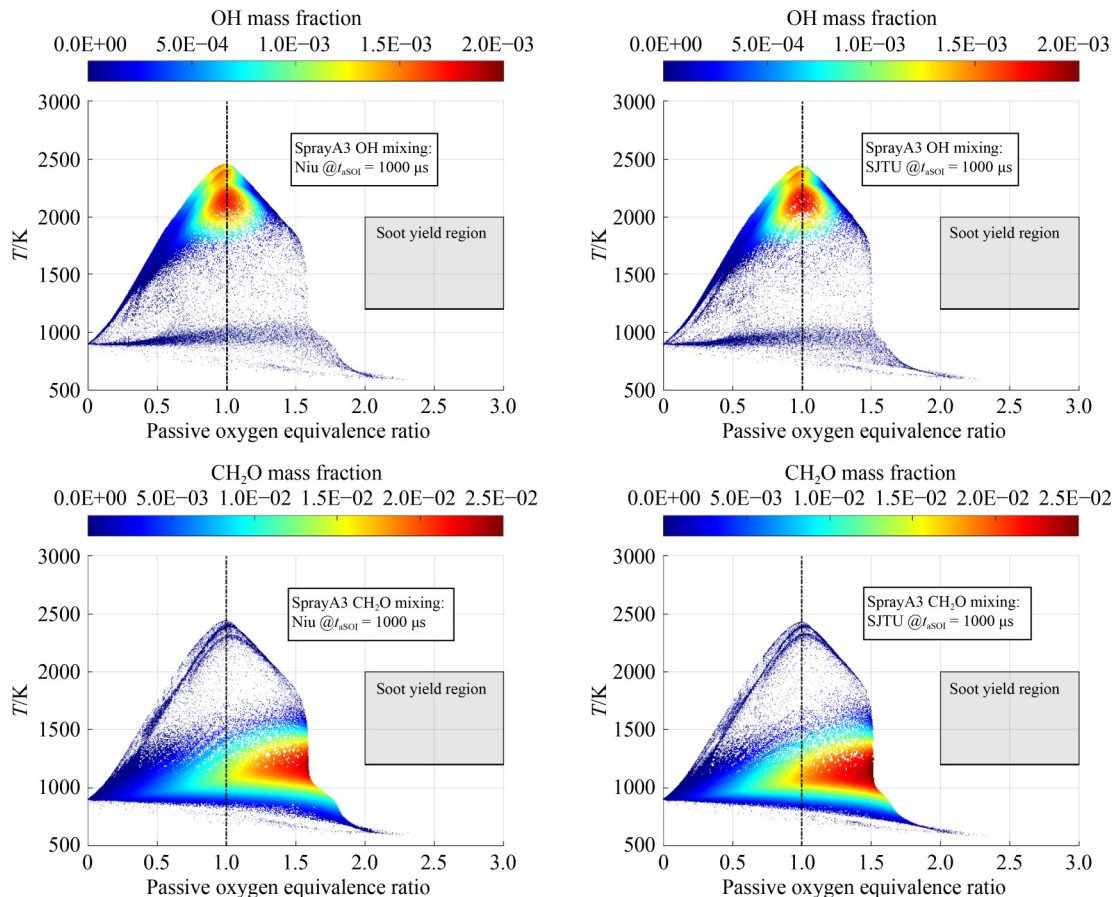
Fig. 19 SprayA3 and OP2 (900 K and 15% O$_2$) (T vs. passive scalar oxygen equivalence ratio for single injection at 1000 μs after SOI). (left) Niu reaction mechanism; (right) SJTU reaction mechanism; (top) colored with OH cell mass fraction and scaled with OH cell mass; (bottom) colored with CH$_2$O cell mass fraction and scaled with CH$_2$O cell mass.

penetration are not influenced by the SJTU mechanism, retaining the already excellent agreement with the measurements achieved with the Niu reaction mechanism.

2) The low-temperature CH$_2$O production is elevated and more concentrated toward the spray center axis. Higher levels of CH$_2$O concentration are present closer to the nozzle. The high-temperature (OH/OH*) reaction activity is slightly increased in the spray axis, likely due to the increased CH$_2$O formation along the spray centerline, constituting a positive trend compared to the measurements. The fuel mechanisms used in this study cannot fully reproduce the experimentally observed high concentration of OH*-radicals near the spray axis.

3) Mixing regimes in the case of the single injection pattern are only slightly affected by the new mechanism toward an even leaner mixing state. In the case of multi-injection patterns, the delayed ignition of the new mechanism influences the high-temperature mixing field. The ignition following the short pilot injection occurs at an ultra-lean condition, not even reaching stoichiometry.

Once the main injection reignites the mixture, the SJTU and Niu mechanisms only show minor differences in terms of mixing, cool-flame, and high-temperature flame distribution.

The tendency of the RANS OME simulation conducted to overestimate the high-temperature reaction activity within the shear layer of spray and ambient air remains a major challenge for research efforts into this topic. The main focus of future investigations will, therefore, be on the role of turbulence modeling in flame morphology by comparing RANS and Large Eddy Simulation (LES) simulations in terms of their impact on ignition locations and high-temperature reaction zones.

Another aspect for future research is the strong OH*-signal intensity observed experimentally at the root of the spray near the nozzle for OME. This behavior cannot be reproduced by the simulations. The differences between the volatile excited OH*-signal and the presumably more stable OH mass fraction within the CFD simulations suggest a possible improvement for reaction mechanisms by incorporating a species that reflects the volatility of excited OH* more adequately.
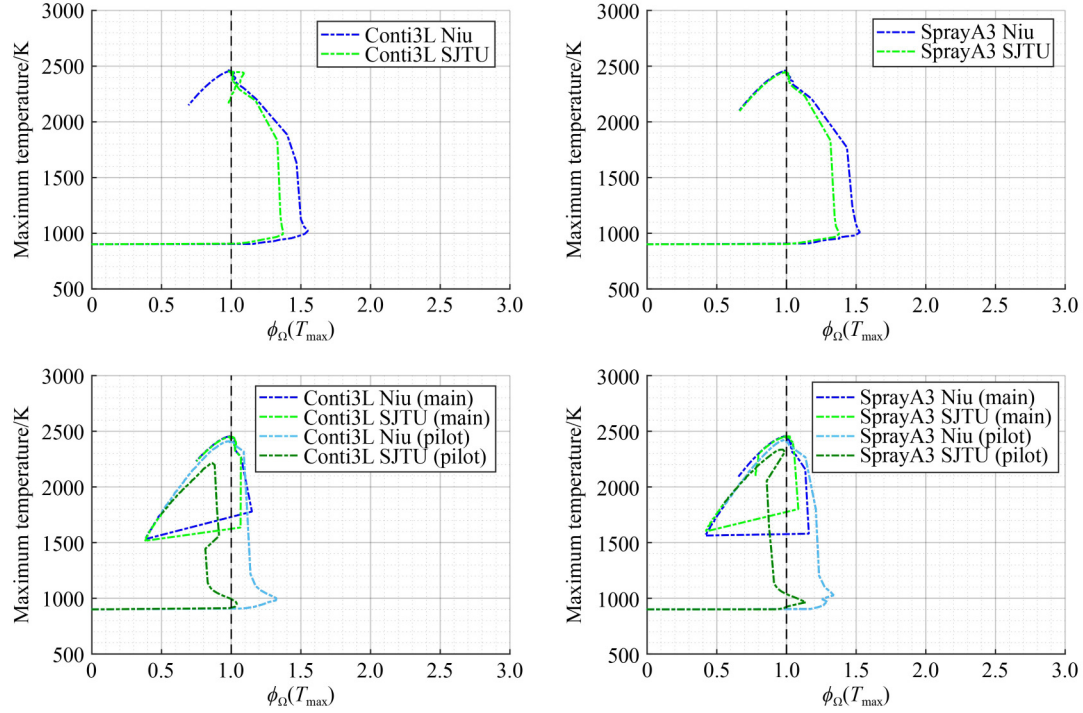
Fig. 20 Maximum temperature versus its corresponding oxygen equivalence ratio at 900 K and 15% O$_2$.
(left) Conti3L injector; (right) SprayA3 injector; (top) single injection; (bottom) multi-injection.

Notations

Abbreviations

C$_2$H$_2$	Acetylene molecule
CFD	Computational fluid dynamics
CH$_2$O	Formaldehyde molecule
CH$_3$O($-$CH$_2$O)$_n$$-CH_3$	Polyoxymethylene dimethyl ether molecule
ECN	Engine Combustion Network
FST	Institute of Fluid System Technology
ID/IDT	Ignition delay timeJSR
KHRT	Kelvin–Helmholtz–Rayleigh–Taylor
LES	Large Eddy Simulation
OH	Hydroxyl radical
OME	Oxymethylene ethers
PODE	Polyoxymethylene dimethyl ethers
OP1	ECN Spray A low temperature conditions (800 K, 22.8 kg/m^3, 15% O$_2$)
OP2	ECN Spray A conditions (900 K, 22.8 kg/m^3, 15% O$_2$)
OP3	ECN Spray A high temperature conditions (1000 K, 22.8 kg/m^3, 15% O$_2$)
OP4	ECN Spray A conditions with multi-injection (900 K, 22.8 kg/m^3, 15% O$_2$
OP5	ECN Spray A high oxygen content conditions (900 K, 22.8 kg/m^3, 21% O$_2$)

RANS	Reynolds averaged Navier–Stokes equations
SJTU	Shanghai Jiao Tong University
SOC	Start of combustion
SOI	Start of injection

Variables

C_A	Injector nozzle hole area contraction coefficient
d	Diameter
k	Pre-exponential factor of reaction
L	Length
$\dot{m}$	Mass flow
p	Pressure
r/R	Radius
S	Sensitivity coefficient
t	Time
T	Temperature
x	Distance
Z	Mixture fraction
Zi	Element mass fraction
ρ	Density
τ	Ignition delay time
ϕ	Equivalence ratio
ϕ_Ω	Oxygen equivalence ratio
Ω	Oxygen ratio

References

1. Huang Z, Zhu L, Li A, et al. Renewable synthetic fuel: Turning carbon dioxide back into fuel. Frontiers in Energy, 2022, 16(2): 145–149

2. Damyanov A, Hofmann P, Geringer B, et al. Biogenous ethers: Production and operation in a diesel engine. Automotive and Engine Technology, 2018, 3: 69–82

3. Liu J, Wang H, Li Y, et al. Effects of diesel/PODE (polyoxymethylene dimethyl ethers) blends on combustion and emission characteristics in a heavy duty diesel engine. Fuel, 2016, 177: 206–216

4. Härtl M, Gaukel K, Pélerin D, et al. Oxymethylene ether as potentially CO_2-neutral fuel for clean diesel engines part 1: Engine testing. MTZ worldwide 2017, 78: 52–59

5. Omari A, Heuser B, Pischinger S. Potential of oxymethyleneether-diesel blends for ultra-low emission engines. Fuel, 2017, 209: 232–237

6. Qiu Z, Zhong A, Huang Z, et al. An experimental and modeling study on polyoxymethylene dimethyl ether 3 (PODE3) oxidation in a jet stirred reactor. Fundamental Research, 2022, 2(5): 738–747

7. Virt M, Arnold U. Effects of oxymethylene ether in a commercial diesel engine. Cognitive Sustainability, 2022, 1(3)

8. Pélerin D, Gaukel K, Härtl M, et al. Potentials to simplify the engine system using the alternative diesel fuels oxymethylene ether OME_1 and OME_{3-6} on a heavy-duty engine. Fuel, 2020, 259: 116231

9. Gelner A D, Rothe D, Kykal C, et al. Particle emissions of a heavy-duty engine fueled with polyoxymethylene dimethyl ethers (OME). Environmental Science: Atmospheres, 2022, 2(2): 291–304

10. Dworschak P, Berger V, Härtl M, et al. Neat Oxymethylene Ethers: Combustion Performance and Emissions of OME_2, OME_3, OME_4 and OME_5 in a Single-Cylinder Diesel Engine. SAE Technical Report 2020-01-0805, 2020

11. Strauß L, Rieß S, Wensing M. Mixture formation of OME_{3-5} and 1-octanol in comparison with diesel-like dodecane under ECN Spray A conditions. Frontiers in Mechanical Engineering, 2023, 9: 1083658

12. Wiesmann F, Strauß L, Rieß S, et al. Numerical and experimental investigations on the ignition behavior of OME. Energies, 2022, 15(18): 6855

13. Wiesmann F, Bauer E, Kaiser S A, et al. Ignition and Combustion Characteristics of OME_{3-5} and N-Dodecane: A Comparison Based on CFD Engine Simulations and Optical Experiments. SAE Technical Report 2023-01-0305, 2023

14. Niu B, Jia M, Chang Y, et al. Construction of reduced oxidation mechanisms of polyoxymethylene dimethyl ethers ($PODE_{1-6}$) with consistent structure using decoupling methodology and reaction rate rule. Combustion and Flame, 2021, 232: 111534

15. ASG. ASG analytik-service. 2022-8-2, available at website of ASG Analytik

16. Pastor J V, García-Oliver J M, Micó C, et al. Experimental study of the effect of hydrotreated vegetable oil and oxymethylene ethers on main spray and combustion characteristics under engine combustion network Spray A conditions. Applied Sciences, 2020, 10(16): 5460

17. ,Chemkin-Pro 15131. San Diego: Reaction Design, 2013

18. Cai L, Jacobs S, Langer R, et al. Auto-ignition of oxymethylene ethers (OME_n, n = 2–4) as promising synthetic e-fuels from renewable electricity: Shock tube experiments and automatic mechanism generation. Fuel, 2020, 264: 116711

19. Hanjalić K, Popovac M, Hadžiabdić M. A robust near-wall elliptic-relaxation eddy-viscosity turbulence model for CFD. International Journal of Heat and Fluid Flow, 2004, 25(6): 1047–1051

20. Popovac M, Hanjalic K. Compound wall treatment for RANS computation of complex turbulent flows. In: Proceedings of the 3rd MIT Conference on Computational Fluid and Solid Mechanics. Boston: Elsevier, 2005

21. Reitz R D. Modeling atomization processes in high-pressure vaporizing sprays. Atomisation Spray Technology, 1987, 3: 309–337

22. Taylor G. The instability of liquid surfaces when accelerated in a direction perpendicular to their planes. I. Proceedings of the Royal Society of London. Series A, Mathematical and Physical Sciences, 1950, 201(1065): 192–196

23. Brenn G, Deviprasath L J, Durst F. Computations and experiments on the evaporation of multi-component droplets. In: Proceedings of the 9th International Conferences on Atomization and Spray Systems. Sorrento, 2003

24. Abramzon B, Sirignano W. Droplet vaporization model for spray combustion calculations. International Journal of Heat and Mass Transfer, 1989, 32(9): 1605–1618

25. O'Rourke P J, Bracco F. Modelling of drop interactions in thick

sprays and a comparison with experiments. Proceedings of the Institution of Mechanical Engineers, Part C: Journal of Mechanical Engineering Science, 1980, 404(80): 101−116

26. Schiller L, Naumann A Z. A drag coefficient correlation. Zeitschrift des Vereins Deutscher Ingenieure, 1933, 77: 318−320

27. Pickett L M, Manin J, Payri R, et al. Transient Rate of Injection Effects on Spray Development. SAE Technical Report 2013-24-0001, 2013

28. CMT. Virtual injection tate generator. 2022–04-07, available at website of Universitat Politècnica de València

29. Peter A, Siewert B, Riess S, et al. Mixture formation analysis of polyoxymethylenether injection. Atomization and Sprays, 2020, 30(11): 843−859

30. Frühhaber J, Peter A, Schuh S, et al. Modeling the Pilot Injection and the Ignition Process of a Dual Fuel Injector with Experimental Data from a Combustion Chamber Using Detailed Reaction Kinetics. SAE Technical Report 2018-01-1724, 2018

31. AVL List GmbH. User Manual for FIRE General Gas Phase Reactions Module Version 2018, 2018

32. Mueller C J. The Quantification of Mixture Stoichiometry When Fuel Molecules Contain Oxidizer Elements or Oxidizer Molecules Contain Fuel Elements. SAE Technical Report 2005-01-3705, 2005

33. ECN. Engine combustion network. 2022-4-7, available at website of Sandia National Laboratories

34. Riess S, Vogel T, Wensing M. Influence of exhaust gas recirculation on ignition and combustion of diesel fuel under engine conditions investigated by chemical luminescence. In: Proceedings of the 13th Triennial Conference on Liquid Atomization and Spray Systems. Tainan, China, 2015

35. Peter A. Charakterisierung der Gemischbildung und Zündung in Diesel- und Dual-Fuel-Brennverfahren. In: Berichte zur Thermodynamik und Verfahrenstechnik. Düren: Shaker Verlag, 2022

36. Tagliante F, Nguyen T M, Dhanji M P, et al. The role of cool-flame fluctuations in high-pressure spray flames, studied using high-speed optical diagnostics and large-eddy simulations. Proceedings of the Combustion Institute, 2023, 39(4): 4871−4879

37. Stiesch G. Modeling Engine Spray and Combustion Processes. Berlin: Springer Heideberg, 2003

38. Pischinger F, Schulte H. Grundlagen und entwicklungslinien der diesel-motorischen brennverfahren. düsseldorf. VDI-Verlag, 1988, 714: 61−93

39. Warnatz J, Maas U, Dibble R W. Combustion: Physical and Chemical Fundamentals, Modeling and Simulation, Experiments, Pollutant Formation. 4th ed. New York: Springer, 2006